A dynamo driven by zonal jets at the upper surface: applications to giant planets

Céline Guervilly, Philippe Cardin, Nathanaël Schaeffer

To cite this version:

Céline Guervilly, Philippe Cardin, Nathanaël Schaeffer. A dynamo driven by zonal jets at the upper surface: applications to giant planets. 2011. hal-00600095v1

HAL Id: hal-00600095
https://hal.science/hal-00600095v1

Preprint submitted on 13 Jun 2011 (v1), last revised 17 Jan 2012 (v2)

A dynamo driven by zonal jets at the upper surface: applications to giant planets

Céline Guervilly, Philippe Cardin & Nathanaël Schaeffer

June 14, 2011

Abstract

We present a dynamo mechanism arising from the presence of barotropically unstable zonal jet currents in a spherical shell. The shear instability of the zonal flow develops in the form of a global Rossby mode, whose azimuthal wavenumber depends on the width of the zonal jets. We obtain self-sustained magnetic fields at magnetic Reynolds numbers greater than 10^3. We show that the propagation of the Rossby waves is crucial for dynamo action. The amplitude of the axisymmetric poloidal magnetic field depends on the wavenumber of the Rossby mode, and then on the width of the zonal jets. We discuss the plausibility of this dynamo mechanism for generating the magnetic field of the giant planets. Our results suggest a possible link between the topology of the magnetic field and the profile of the zonal winds observed at the surface of the giant planets. For narrow Jupiter-like jets, the poloidal magnetic field is dominated by an axial dipole whereas for wide Neptune-like jets, the axisymmetric poloidal field is weak.

1 Introduction

The zonal (i.e. axisymmetric and azimuthally directed) jet streams visible at the surface of the giant planets are a persistent feature of the fluid dynamics of these planets (figure 1). The gas giants (Jupiter and Saturn) display a strong eastward equatorial jet, extending to latitudes ±20° with a peak velocity exceeding 100m/s on Jupiter (Porco et al., 2003), and to latitudes ±30° with a peak velocity exceeding 400m/s on Saturn (Sanchez-Lavega et al., 2000). At higher latitudes, alternating prograde (eastward) and retrograde (westward) jets of smaller amplitude are observed extending all the way up to the poles.

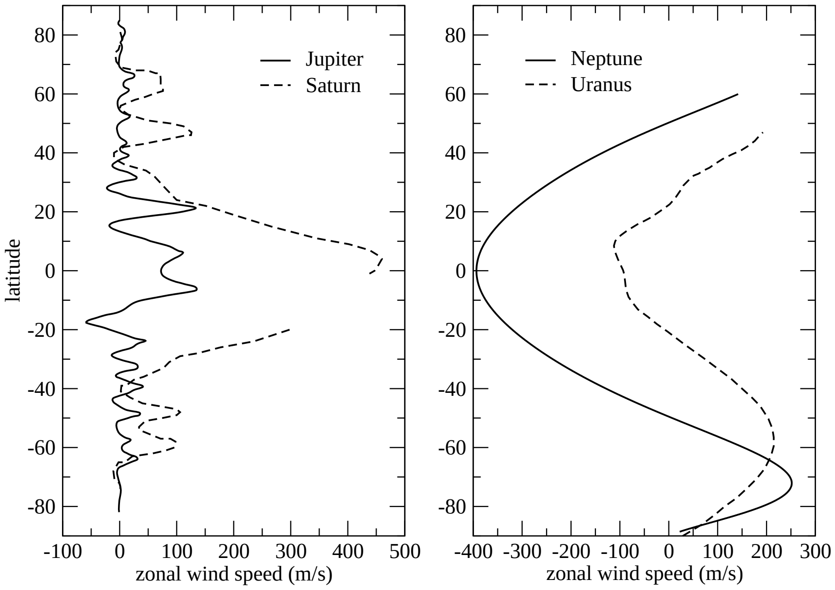

Figure 1: Zonal velocity measured at the surface in the planet's mean rotating frame for each of the four giants by tracking cloud features in the outer weather layer. Profiles adapted from Porco et al. (2003), Sanchez-Lavega et al. (2000), Sromovsky et al. (2001) and Sromovsky and Fry (2005).

These profiles are fairly symmetric with respect to the equator. On the ice giants (Uranus and Neptune) the picture is rather different. A very intense retrograde equatorial current is present with maximum velocity of 100m/s on Uranus (Sromovsky and Fry, 2005) and 400m/s on Neptune (Sromovsky et al., 2001). At higher latitudes, a single prograde jet of large amplitude is present in each hemisphere. Several decades of observations show that these zonal flows remain approximately steady (Porco et al., 2003).

The origin of these zonal flows and the associated question of the depth to which they extend into the planets' interiors have been areas of active research in rotating fluid dynamics for several decades (*e.g.* Jones and Kuzanyan, 2009, and references therein; see also the review by Vasavada and Showman, 2005). In particular, several model have been proposed to explain the zonal wind pattern of Jupiter, and can be categorised into two main classes: weather layer models and deep convective layer models. The former assume that the zonal flows are produced in a shallow stably stratified region near cloud level. These models are able to reproduce the high latitude structures with alternating eastward and westward jets and a strong equatorial current (*e.g.* Williams, 1978; Cho and Polvani, 1996). These models intrinsically produce a retrograde equatorial jet (Yano et al., 2003), so they provide a plausible explanation for the retrograde equatorial current of the ice giants but not for the prograde flow observed on gas giants. A parametrised forcing such as a strong equatorially-localised baroclinicity is required to force a shallow system to produce a prograde equatorial jet (Williams, 2003). The second class of model is deep convection models which simulate most or all of the whole 10^4km-thick molecular hydrogen (H_2) layer (Busse, 1976; Christensen, 2001, 2002; Manneville and Olson, 1996). The presence of deep convection is inferred from the observation that the atmospheres of the major planets emit more energy by long-wave radiation than they absorb from the Sun. Consequently their atmospheres must receive additional heat supplied by the interior of the planet. Recent numerical models using either a Boussinesq approximation (Heimpel et al., 2005) or an anelastic approximation (Jones and Kuzanyan, 2009) with sufficiently low Ekman numbers (i.e. strong rotational effect compared with viscous dissipation) display alternating zonal jets at high latitudes. A strong eastward equatorial jet is a robust feature of these models where the Coriolis force dominates buoyancy, in good agreement with the gas giant observations. Interestingly, deep convection models suggest that the zonal velocity generated by the non-linear interaction of the convective motions (*i.e.* the motions directly forced by buoyancy) is roughly geostrophic, that is, invariant along the direction of the rotation axis. This feature is also present in strongly compressible models provided that the Ekman number is small enough, despite the increase of density with depth yielding ageostrophic convective motions (Jones and Kuzanyan, 2009; Kaspi et al., 2009). When the convection is more vigorous such that the buoyancy force overcomes the Coriolis force, 3D turbulence homogenizes angular momentum; a retrograde jet forms in the equatorial region and a single strong prograde jet forms in the polar region, in good agreement with the ice giant observations (Aurnou et al., 2007).

Another feature of the giant planets is their strong magnetic fields (figure 2). The magnetic field observed for gas and ice giants are drastically different (see for instance the recent review by Russell and Dougherty, 2010). Jupiter and Saturn have a main axial dipole component (corresponding to $l = 1$, $m = 0$ on figure 2), a feature shared with the Earth for instance (Yu et al., 2010; Burton et al., 2009). Neptune and Uranus, on the other hand, have strong non-axial multipolar components (corresponding to $l = 2, 3$ on figure 2) compared with the axial dipole component (Connerney et al., 1991; Herbert, 2009). The magnetic field is generated in the deep, electrically conducting regions of the planets' interior: a metallic hydrogen layer for Jupiter and Saturn (Nellis et al., 1999; Guillot, 2005, and references therein) and an electrolyte layer composed of water, methane and ammonia (Hubbard et al., 1991; Nellis et al., 1997) or superionic water (Redmer et al., 2011) for Uranus

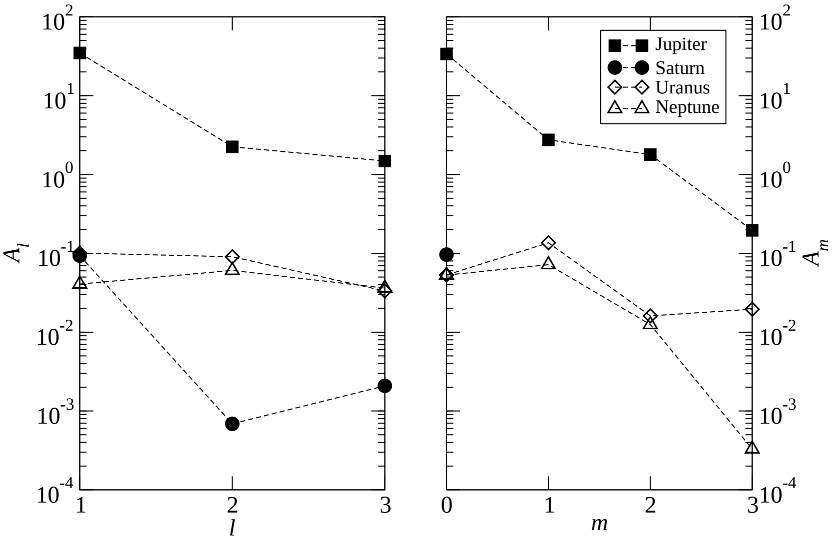

Figure 2: Spectra of the magnetic field squared amplitude at the planetary radius for degrees l and order m up to 3 obtained from inversion models of the magnetic measurements. The squared amplitude for a given degree l is $A_l = \sum_{m=0}^{l}(l+1)\left[(g_l^m)^2 + (h_l^m)^2\right]$ using a Schmidt normalisation for the spherical harmonics. The squared amplitude for a given mode m is $A_m = \sum_{l=m}^{l_{max}}(l+1)\left[(g_l^m)^2 + (h_l^m)^2\right]$. g_l^m and h_l^m are the Gauss coefficients in gauss. After Yu et al. (2010) (Model Galileo 15), Burton et al. (2009) (Cassini measurements), Connerney et al. (1991) (model O_8) and Herbert (2009) (AH_5 model from magnetic observations and auroral data).

and Neptune.

Numerical models of convective dynamos in rapidly rotating spherical shells typically produce axial dipolar dominated magnetic fields for moderate Rayleigh numbers and low Ekman numbers (*e.g.* Olson et al., 1999; Aubert and Wicht, 2004; Christensen and Wicht, 2007). To explain the unusual magnetic fields of Uranus and Neptune, models using peculiar parameter regimes or different convective region geometries have been proposed. The latter models show that a numerical dynamo operating in a thin shell surrounding a stably-stratified fluid interior produces magnetic field morphologies similar to those of Uranus and Neptune (Hubbard et al., 1995; Holme and Bloxham, 1996; Stanley and Bloxham, 2006). Gómez-Pérez and Heimpel (2007) obtain weakly dipolar and strongly tilted dynamo magnetic fields when high magnetic diffusivity are used (or equivalently small electrical conductivity). Their results show that these peculiar fields are stable in the presence of strong zonal circulation and when the flow has a dominant effect over the magnetic fields. This feature is also emphasised by Aubert and Wicht (2004) who find stable equatorial dipole solutions with a weak magnetic field strength and low Elsasser number (measure of the relative importance of the Lorentz and Coriolis forces) for moderately low Ekman numbers. They argue that the magnetic field geometry of the equatorial dipole solution is incompatible with the columnar convective motions and thus this morphology is stable only when the Lorentz force is weak.

The dichotomies observed in the magnetic fields and in the zonal wind profiles of the giant planets are striking. Up to now no study has tried to relate them directly, probably because the former is a feature of the deep interior whereas the latter is a characteristic of the surface. However, if some mechanism is able to transport angular momentum from the surface down to the deep, fully conducting region then the zonal motions may influence the generation of the magnetic field. In the non-magnetic deep convection models (Heimpel et al., 2005; Jones and Kuzanyan, 2009), zonal motions extend geostrophically throughout the electrically insulating molecular hydrogen layer down to the bottom of the model. On the other hand, due to the possible rapid increase of electrical conductivity with depth in the outer region, Liu et al. (2008) argued that the ohmic dissipation produced by geostrophic zonal motions shearing dipolar magnetic field lines would exceed the luminosity measured at the surface of Jupiter if the vertical extent of this geostrophic zonal motions exceeds 4% of the planet radius. However, the argument of Liu et al. (2008) is purely kinematic, that is no magnetic force acts on the flow. In a self-consistent magnetohydrodynamic model, the zonal flow would adjust toward a non-geostrophic state due to the action of magnetic forces if the electric conductivity of the fluid is significant

(Glatzmaier (2008), see the non-linear numerical simulations of convectively-driven dynamos of Aubert (2005)). In this case, angular momentum may be transported along the magnetic field lines leading to a so-called "Ferraro state". This state minimises the ohmic dissipation produced by the shearing of the poloidal magnetic field by the zonal flow as angular velocity contours are aligned with the poloidal magnetic field lines. Both scenario, either geostrophic zonal balance or Ferraro state, imply the existence of multiple zonal jets of significant amplitude at the top of the fully conducting region beneath. The plausibility of each scenarios depends on the radial profile of electric conductivity, which is currently not well constrained within the giant planets (Nellis et al., 1999).

The idea of the work presented in this paper is that these zonal jets may exert, by viscous or electromagnetic coupling, an external forcing at the top of the deeper conducting envelope. From previous studies (Schaeffer and Cardin, 2006; Guervilly and Cardin, 2010) we know that the viscous coupling between a differentially rotating boundary and a low-viscosity electrically conducting fluid can generate a self-sustained magnetic field in different geometries. In order to test the plausibility of a dynamo driven by this coupling in isolation, we use an incompressible 3D numerical dynamo model with a zonal velocity profile imposed at the top of a spherical shell containing a conducting fluid. We use a dynamical approach, that is non-linear interactions between the flow and the magnetic field are taken into account; therefore any motion is free to adopt a three-dimensional structure as long as it satisfies the imposed viscous boundary conditions.

In order to assess the role of the zonal wind profile on the topology of the sustained magnetic field, we use a Jupiter-like and a Neptune-like zonal wind profiles. In the giant planets, as in rocky planets, it is usually assumed that the dynamo mechanism is driven by convective motions. The giant planets display a strong surface heat flux (with the exception of Uranus) meaning that heat transfer is efficient in the interior of the planet and thus mostly due to convection (Guillot and Gautier, 2007, and references therein). Here we want to assess the efficiency of zonal velocity forcing alone, so we do not model convective motions.

The first goal of this work is to quantify what amplitude of the zonal wind *inside* the conducting layer is needed to trigger the dynamo instability, so we do not model the exact or realistic coupling between the molecular hydrogen upper layer and the deep, electrically conducting region. Our second goal is to test to what extent the pattern of the zonal flow imposed at the top of the conducting layer influences the topology of the self-sustained magnetic field.

We first describe the model and the numerical method used (section 2). Then we present numerical results from simulations in the non-magnetic case (section 3) followed by results from dynamo simulations (section 4).

2 Model

We model the deep conducting layer of the giant planets as a thick spherical shell. At the top of the conducting layer we impose an axisymmetric azimuthal velocity to represent the zonal flow generated in the overlying envelope.

The shell rotates around the z-axis at the imposed rotation rate Ω. The aspect ratio is $\gamma = r_i/r_o$ where r_i is the inner sphere radius, corresponding to a rocky core, and r_o the outer sphere radius, corresponding to the top of the fully conducting region. The fluid is assumed incompressible with constant density ρ and constant temperature, that is, no convective motions are computed. The assumption of incompressibility is made for simplicity, although the pressure scale height H_p at the depths of the conducting layer is roughly 8000km (Guillot et al., 2004), that is, about 1/5 of the thickness of the layer. The effects of compressibility may well play a role in the dynamics of the conducting regions (see for instance Evonuk and Glatzmaier, 2004).

For simplicity we model the angular momentum coupling with the external zonal flow as a rigid boundary condition for the velocity at the outer boundary, rather than as a shear stress condition. The flow is driven through a boundary forcing rather than a volume forcing to avoid directly imposing bidimensionality to the velocity field. As we are interested in the bulk magnetohydrodynamical process, the exact nature of the coupling (electromagnetic or viscous, shear stress or rigid) with the upper molecular hydrogen layer is not crucial for our study. We discuss the implication of the choice of the rigid boundary condition in section 3

The radial profile of electrical conductivity is not well constrained in the gas giants. In particular the existence of a first order or continuous transition between the molecular and metallic hydrogen phase is still an open question, although high-pressure experiments are in favour of a continuous transition (Nellis et al., 1999). We choose to model the outer boundary as electrically insulating to simplify the coupling between the layers. The conductivity is assumed constant throughout the whole modelled conducting layer.

The existence of a rocky core at the centre of the giant planets is uncertain and depends on the poorly constrained composition of the planet. Estimates for the core mass are $0 - 14m_\oplus$ for Jupiter (total mass $318m_\oplus$), $6 - 17m_\oplus$ for Saturn (total mass $95m_\oplus$) and $0 - 4m_\oplus$ for Uranus and Neptune (total mass $15m_\oplus$ and $17m_\oplus$ respectively) where $m_\oplus$ denotes the mass of the Earth (Guillot, 2005). If present, the rocky cores are therefore believed to be small.

Following the interior model of Jupiter proposed by Guillot et al. (1994) we use an aspect ratio $r_i/r_o = 0.2$ for all the simulations performed. The inner core is assumed to be electrically conducting, with the same conductivity as the fluid in the conducting layer. We did not carry out simulations with an insulating core as the effect of the conductivity of the inner core on the dynamo mechanism is believed to be small (Wicht, 2002). The velocity boundary condition is no-slip at the inner boundary.

As we do not model the molecular hydrogen layer, we assume zonal geostrophic balance within this envelope. The amplitude of the zonal motions at the outer boundary of our model is therefore the same as the surface winds. If we had instead assumed a Ferraro state, the amplitude of the zonal motions would be reduced and the profile would be distorted along the magnetic field lines, although the characteristics of the zonal jet (narrow or wide, relative amplitude) would presumably not be altered very much. We use two different synthetic azimuthal velocity profiles for the boundary forcing imposed at the top: a multiple jet profile for the gas giants with a profile based on Jupiter's surface zonal winds (hereafter profile J) and a 3-band profile based on Neptune's surface zonal winds (profile N).

For Jupiter, we use the profile given in Wicht et al. (2002)

$$\mathbf{U} = U(s)\mathbf{e}_\phi = U_0 \frac{s}{r_0 \cos(n_0 \pi)} \cos\left(n_0 \pi \frac{s - r_0}{r_s - r_0}\right) \mathbf{e}_\phi, \tag{1}$$

where $s = r\sin\theta$, r_s is the surface radius of the planet and $U_0 = U(r_0, \theta = \pi/2)$. n_0 controls the numbers of jets. The profile at the radius r_s best matches the observed profile at the surface for $n_0 = 4$ (figure 3). The profile $U(r_o, \theta)$ is used to drive the flow at the top of our simulated metallic hydrogen layer (figure 3). The ratio $\gamma_s = r_s/r_o$ determines the U profile at r_o. We choose $\gamma_s = r_s/r_o = 1/0.8 = 1.25$ following Guillot et al. (1994).

For the Neptune-like profile, we use the zonal velocity profile measured at the surface of Neptune, approximated by a polynomial of order 10 in latitude. We project this surface velocity profile geostrophically down to r_o using $\gamma_s = 1/0.85 = 1.18$ (Hubbard et al., 1991) (figure 3).

The velocity $\mathbf{u}$ is scaled by U_0, the absolute value of the azimuthal velocity imposed at the equator of the outer sphere r_o. The lengthscale is the radius of the outer sphere r_o. The magnetic field $\mathbf{B}$ is scaled by $\sqrt{\rho\mu_0 r_o \Omega U_0}$ where ρ is the fluid density and μ_0 is the vacuum magnetic permeability.

We numerically solve the momentum equation for an incompressible fluid,

$$Re\frac{\partial \mathbf{u}}{\partial t} + Re\left(\mathbf{u}\cdot\boldsymbol{\nabla}\right)\mathbf{u} + \frac{2}{E}\mathbf{e_z}\times\mathbf{u} = -\boldsymbol{\nabla}p + \boldsymbol{\nabla}^2\mathbf{u} + \frac{1}{E}\left(\boldsymbol{\nabla}\times\mathbf{B}\right)\times\mathbf{B}, \tag{2}$$

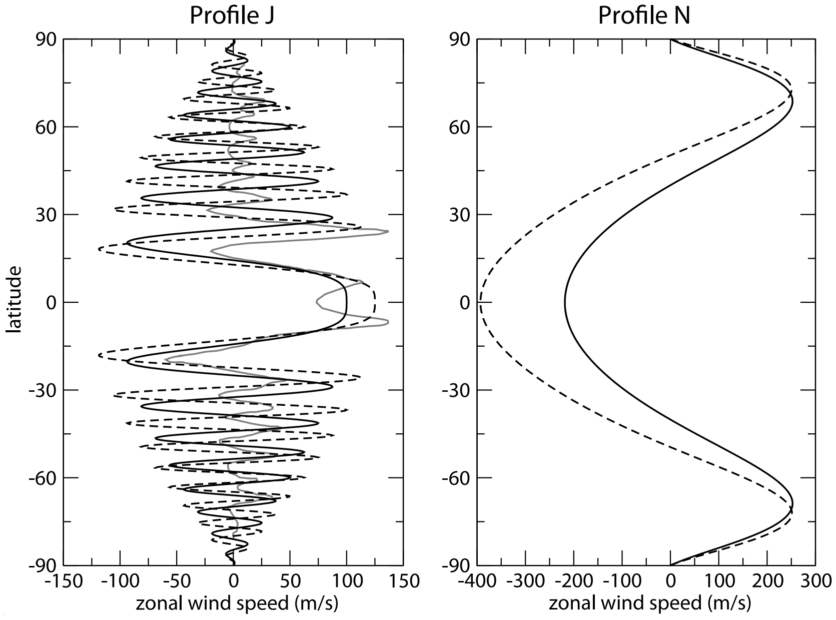

Figure 3: Zonal velocity profile imposed at the surface of the model J (left) and the model N (right) (solid lines). Both profiles are obtained by assuming that the zonal velocities are geostrophic for $r_s > r > r_o$ and using the profile represented by a dashed line at the surface of the planet ($r = r_s$): model J, profile (1) with $n_0 = 4$, $\gamma_s = r_s/r_o = 1.25$ and $U_0 = 100$; model N: polynomial fit of order 10 in latitude of the zonal wind profile measured at the surface of Neptune (figure 1) with $\gamma_s = 1/0.85 = 1.18$. For comparison the zonal wind profile measured at the surface of Jupiter is plotted in gray.

the continuity equation,

$$\boldsymbol{\nabla} \cdot \mathbf{u} = 0, \tag{3}$$

and the magnetic induction equation,

$$\frac{\partial \mathbf{B}}{\partial t} = \boldsymbol{\nabla} \times (\mathbf{u} \times \mathbf{B}) + \frac{1}{RePm} \boldsymbol{\nabla}^{\mathbf{2}} \mathbf{B}, \tag{4}$$

$$\boldsymbol{\nabla} \cdot \mathbf{B} = 0, \tag{5}$$

where p is the dimensionless pressure, which includes the centrifugal potential.

The Reynolds number $Re = r_o U_0/\nu$ parametrises the mechanical forcing exerted on the system by controlling the amplitude of the zonal velocity. The magnetic Prandtl number $Pm = \nu/\eta$ measures the ratio of viscous to magnetic diffusivities. Note that the magnetic Reynolds number Rm is defined as $Rm = RePm$. The Ekman number $E = \nu/(\Omega r_o^2)$ measures the importance of the viscous term over the Coriolis force. The Rossby number $Ro = ReE = U_0/(\Omega r_o)$ is the ratio of inertial force to Coriolis force. Note that hereafter each mention to the Rossby number corresponds to this "forcing" Rossby number and not a local Rossby number based on rms velocities. The results presented in this paper were obtained with the PARODY code, a fully three-dimensional and non-linear code, derived from Dormy (1997) by Aubert, Cardin, Dormy in the dynamo benchmark (Christensen et al., 2001), and parallelised and optimised by J. Aubert and E. Dormy. The velocity and magnetic fields are decomposed into poloidal and toroidal scalars and expanded in spherical harmonic functions in the angular coordinates with l representing the latitudinal degree and m the azimuthal order. A finite difference scheme is used on an irregular radial grid (finer near the boundaries to resolve the boundary layers). A Crank-Nicolson scheme is implemented for the time integration of the diffusion terms and an Adams-Bashforth procedure is used for the other terms.

3 Dynamics without the magnetic field

For a rapidly rotating system in which the Coriolis force exactly balances the pressure force, the Proudman-Taylor constraint states that the flow is z-invariant and follows geostrophic contours. For an incompressible fluid trapped into a bounded container, these geostrophic contours correspond to surfaces of equal height. In a sphere the only geostrophic motions are azimuthal and axisymmetric. In the giant planets' conducting envelopes, the Ekman number is about 10^{-16} and the Rossby number is much smaller than 1 (Guillot et al., 2004). In the absence of the magnetic field, we expect the Proudman-Taylor constraint to hold for large scale motions. As we want to reach the dynamical regime in which the flow is strongly geostrophic, the use of small Ekman and Rossby numbers is required. We carried out simulations for $10^{-5} > E > 10^{-6}$ for the model J and $10^{-5} > E > 5 \times 10^{-6}$ for the model N. The Rossby numbers are always smaller than 0.1. For the profile J, in cases of low Ekman numbers ($E \leq 2 \times 10^{-6}$), we imposed longitudinal symmetry by calculating only the harmonics of a chosen order m_s. The required resolution for $E = 10^{-6}$ is 500 points on the radial grid and $l = 580$ spherical harmonics degrees.

3.1 Axisymmetric flow

When the imposed boundary forcing is small enough, *i.e.* when the Rossby number Ro is less than a critical value Ro_c, the flow is axisymmetric and predominantly azimuthal (figure 4). The zonal jets imposed at the outer boundary extend into the volume along lines parallel to the axis of rotation.

The use of no-slip boundary conditions yields a differential rotation between the boundary and the bulk of the fluid. This differential rotation is accommodated across viscous Ekman boundary layers, which scale as $(E/\cos\theta)^{1/2}$, where θ is the colatitude. By Ekman pumping, viscous forces within the Ekman layers drive axial motions of order $E^{1/2}$ within the bulk of the fluid (figure 4). These meridional circulations advect angular momentum from the boundary layer into the bulk of the fluid and cause the jets to spread on a shorter timescale than by viscous spreading. At low latitudes, the Ekman layer is thicker so the Ekman pumping is stronger, yielding to a more efficient driving of the zonal motions in the bulk by the outer boundary layer. For the model J (figure 5(a)), the zonal velocity in the bulk relative to that imposed at the outer boundary is noticeably weaker for the inner jets than for the outer jets. When E decreases this effect is less marked, and in the $E \to 0$ limit we expect the basic zonal velocity to be perfectly geostrophic in the whole volume. Therefore, in our viscous calculations, the onset of the hydrodynamic instability (based on the imposed forcing at the top) is overestimated (described in the next section). The comparison between the zonal velocity just below the Ekman layer and in the equatorial plane (figure 5) significantly shows that the zonal velocity is geostrophic in the bulk of the fluid (outside of the boundary layers). For the model N (figure 5(b)), the zonal jets are wider, so the zonal flow already displays a strong geostrophic structure at $E = 10^{-5}$. Note that the azimuthal velocity has to match the

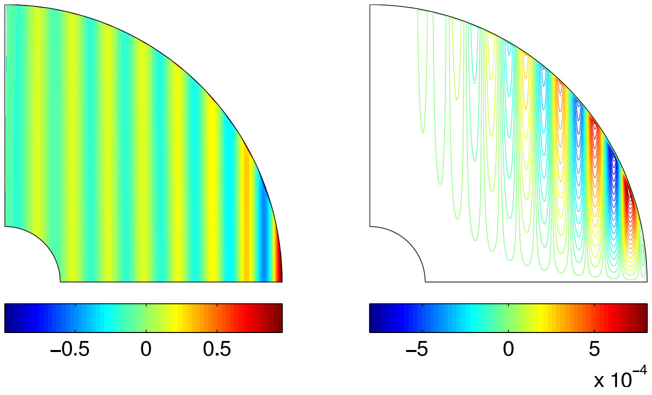

(a) Model J

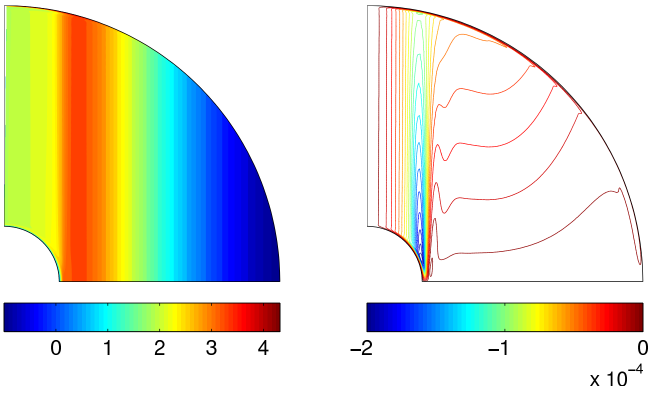

(b) Model N

Figure 4: Angular velocity $u_\phi/(r\sin\theta)$ (left) and streamlines of the meridional circulation (isocontours of $\psi = r\sin\theta\frac{\partial u_p}{\partial\theta}$ with u_p the velocity poloidal scalar) (right) of the axisymmetric flow in a upper meridional plane. Positive (negative) values of ψ mean anticlockwise (clockwise) motions. The parameter for the simulations are $E = 5\times10^{-6}$ and $Ro = 0.015$ for the model J (a) and $E = 10^{-5}$ and $Ro = 0.02$ for the model N (b).

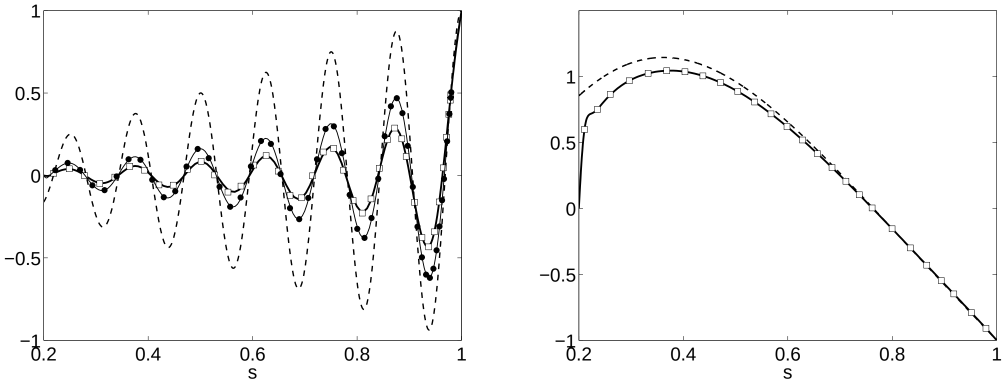

(a) Model J (b) Model N

Figure 5: Zonal velocity in the equatorial plane for subcritical numerical simulations (solid lines) compared to the zonal velocity at radius $r = 0.98r_o$ (symbols) and imposed velocity at the top (dashed line) both geostrophically projected in the equatorial plane for (a) the model J ($E = 5 \times 10^{-6}$ (bold solid line and open squares) and $E = 10^{-6}$ (thin solid line and black circles)) and (b) the model N ($E = 10^{-5}$ (bold solid line and open squares)).

no-slip boundary condition of the inner wall at $r = r_i$ through a Stewartson layer (Stewartson, 1957, 1966). The meridional circulation within the tangent cylinder to the inner core is associated with this Stewartson layer (figure 4(b)).

3.2 Non-axisymmetric motions

3.2.1 Model J

Rossby wave at the onset When the boundary forcing (measured by Ro) becomes greater than a critical value Ro_c, the axisymmetric basic flow becomes unstable to non-axisymmetric shear instability. The saturated instability takes the form of azimuthal necklaces of cyclonic and anticyclonic vortices aligned with the axis of rotation, nearly z-independent and drifting eastward (figure 6). Close to the threshold, the radial extension of the pattern is large and occupies almost half of the gap. The pattern drifts with the same speed over its whole radial extension, even though the advection by the zonal flow velocity varies with s, implying that it is a single wave.

Wicht et al. (2002) studied the linear stability of the imposed zonal flow (1) in a spherical shell modelling the insulating molecular hydrogen layer of Jupiter (aspect ratio 0.8). For $E = 10^{-4}$ they found nearly bidimensional instabilities that they described as drifting columns aligned with

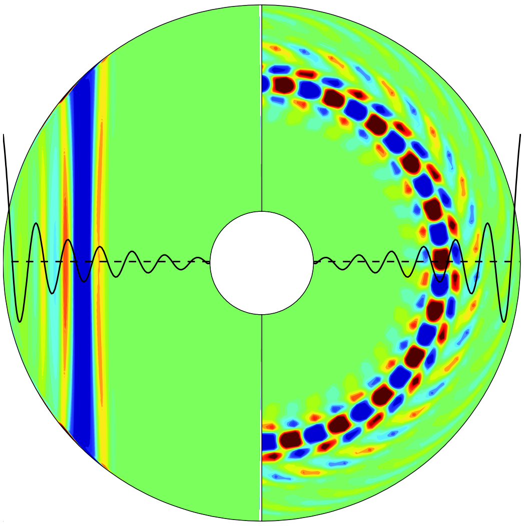

Figure 6: Non-zonal axial vorticity in the equatorial plane (right) and in a meridional slice (left) for the model J at $E = 4 \times 10^{-6}$ and $Ro = 1.01 Ro_c$ (blue: negative and red: positive). The black line represents the zonal velocity in the equatorial plane.

the rotation axis and similar to convective solutions. Although they do not identify these instabilities as waves, their characteristics are very similar to the ones obtained with our non-linear model.

The nearly z-invariant structure and the prograde drift are two characteristics of Rossby waves propagating in a spherical container. The dispersion relation for the Rossby wave given by a local linear analysis is (*e.g.* Finlay, 2008)

$$\omega_{rw}(s) = -2\Omega\beta \frac{m/s}{k_s^2 + (m/s)^2}, \tag{6}$$

where $\beta = h^{-1}(dh/ds) = -s/(r_o^2 - s^2)$ is related to the slope of the upper boundary of the spherical container of height h. k_s and m/s are the radial and azimuthal wavenumbers respectively. For different E, we computed the frequency ω of the propagating wave observed in our numerical simulations. The theoretical Rossby wave frequency ω_{rw} can be calculated at a given radius assuming $k_s \approx m/s$ and using the wavenumber m obtained from the numerical simulation. We always find that $\omega_{rw}(s_1) < \omega < \omega_{rw}(s_2)$ where $s_1 = 0.56$ ($s_2 = 0.87$) is the smallest (resp. largest) radius where a significant vorticity associated with the presence of the wave can be seen in the numerical calculations. This strongly indicates that the shear instability occurs as a Rossby wave.

The velocity of the zonal flow U enters the dispersion relation of the Rossby wave

$$\omega(s) = \omega_{rw}(s) + U(s)\frac{m}{s} \tag{7}$$

where $\omega_{rw}(s)$ is given by equation (6) for a Rossby wave that propagates in the case $U = 0$. As reported earlier, $\omega(s)$ is constant in our numerical calculations so $\omega_{rw}(s)$ must adapt in the s-direction for the wave to be coherent. In a prograde jet $U > 0$, ω_{rw} must decrease, which requires a local increase in k_s in equation (6) and so a local decrease in the radial lengthscale, which can be observed in figure 6.

In a local approximation that neglects the curvature terms, a criterion of instability of barotropic shear flows has been derived by Ingersoll and Pollard (1982) for an anelastic model in a full rotating sphere and by Kuo (1949) for thin stably stratified "weather" layers. Using an inviscid Boussinesq model and for barotropic instability of a zonal flow U in a sphere, this necessary condition implies a change of sign of a quantity Δ at the critical radius:

$$\Delta = 2\beta - Ro\frac{d\zeta}{ds}, \tag{8}$$

where ζ is the vorticity of the zonal flow,

$$\zeta = \frac{dU}{ds} + \frac{U}{s}. \tag{9}$$

Note that the curvature terms have been taken into account here. In a sphere, β is negative. Consequently, the zonal velocity profile becomes first unstable where the gradient of zonal vorticity is maximum and negative. Then for a profile U of sinusoidal form, the first shear instability occurs at the maximum of the prograde jets. In a numerical study of an axisymmetric shear layer (Stewartson layer) produced by differential rotation in a spherical container, Schaeffer and Cardin (2005) found that the destabilisation of the shear layer into Rossby waves occurs where the vorticity gradient is maximum, in agreement with (8). As their U profile presents a sharp discontinuity, the maximum of $d\zeta/ds$ nearly coincides with the maximum of the zonal velocity shear dU/ds. This is not the case when considering a sinusoidal profile and thus the shear instability occurs, perhaps surprisingly, at the minimum of the zonal velocity shear.

For small enough Ekman number (in practice $E < 5 \times 10^{-6}$), the critical wavenumber m_c of the Rossby mode is independent of E. The radial lenghtscale is determined by the width of the jet and the vortices are roughly circular in the equatorial plane (figure 6) showing that m_c is controlled by the width of the jets. The theoretical critical Rossby number obtained from applying the criterion (8) to the profile (1) imposed at the top of the model, is 0.0011, in good agreement with the critical Rossby number obtained numerically for small Ekman numbers (see figure 2 and A). Not that for the large radial extent instabilities we observe, the local criterion cannot predict their location, as their maximum amplitude is located in a retrograde zonal jet (see figure 6) whereas the local criterion would predict an onset in a prograde jet. A detailed study of the onset of the hydrodynamic instability can be found in A.

The characteristic time of the Rossby wave is $\tau_{rw} = 1/\omega$. At the instability threshold, the numerical simulations give $\tau_{rw} \approx 18\Omega^{-1}$ for $E < 5 \times 10^{-6}$. The ratio ω_{rw}/Ω is constant according to the dispersion relation (6) for a given m and s. The timescale of the zonal jets is $\tau_{zj} = r_o/U_0 = \Omega^{-1}/Ro$. For $Ro = 0.01$, we have $\tau_{zj} > \tau_{rw}$: the Rossby wave propagation is faster than the advection of the fluid by the zonal flow. The turnover time of a fluid particle trapped in a Rossby wave is $\tau_{to} = l/V_s$ where l is the typical radial displacement of the particle and V_s the typical cylindrical radial velocity of the particle. At $Ro = 1.01Ro_c$, V_s is typically $10^{-2}U_0$. In a rough approximation we use $l = \delta$ where δ is the width of the jets, $\delta \approx 0.1r_o$ for the profile J. Then we obtain $\tau_{to} \approx 0.1r_o/(10^{-2}U_0) \approx 10Ro^{-1}\Omega^{-1} \approx 10^3\Omega^{-1}$: the turnover time of the particle is much longer than the timescale of the wave. Consequently the particle oscillates rapidly as the wave propagates and is slowly advected by the zonal flow. In practice the radial displacement l is typically smaller than δ and so the turnover time is slightly overestimated here.

Supercritical regime When the Rossby number is increased in the supercritical regime, the other prograde jets will eventually become unstable. A second Rossby wave appears in the weakly supercritical regime, at $Ro = 1.06Ro_c$ for $E = 5 \times 10^{-6}$. The second wave occurs outward from the first wave (*i.e.* the wave appearing for $Ro = Ro_c$) (figure 7(a)). The maximum of the second wave velocity is located in the retrograde zonal jet adjacent to the one carrying the first wave maxima. The azimuthal wavenumber of the second wave ($m = 22$) is slightly larger than the one of the first wave ($m = 21$) since the radial and azimuthal lengthscales are roughly equal and its location is at a larger radius whereas the width of the jet remains unchanged. The second wave propagates faster, in agreement with the Rossby wave dispersion relation (6). It is well known that barotropic instabilities tend to broaden and weaken narrow jets by redistributing potential vorticity (see for instance Pedlosky, 1979). The Rossby waves provoke their own saturation by smoothing the jets. For this slightly supercritical regime the zonal flow profile is only weakly modified. Upon further increasing the forcing ($Ro = 2.94Ro_c$), several Rossby waves of different wavenumbers superpose and interact (figure 7(b)). The structure of the waves is still mainly bidimensional. The modification of the zonal jets by the waves affects their whole height in the bulk of the fluid so they remain essentially geostrophic except in the viscous boundary layers. The typical cylindrical radial velocity is $V_s \approx 0.1U_0$ and the Rossby number is 0.05 so the turnover time is about $20\Omega^{-1}$ assuming that the radial displacement $l = \delta$, about the same order of magnitude as the timescale of the zonal jets.

In figure 8(a) the time-averaged zonal flow in the equatorial plane is plotted for different Ro up to $Ro = 5.88Ro_c$. As the forcing is increased, the Rossby waves gradually reduce the jet strength and broaden the jet width. For $Ro = 2.94Ro_c$, the retrograde jet at $s = 0.81$ has been mostly destroyed leading to the widening of the zonal jet width. We note that the zonal flow becomes mostly westward for the strongest forcings. The zonal flow located at $s > 0.9$ does not visibly undergo a decrease of its amplitude as the threshold to destabilise the outermost jets is high due to the large slope (related to β in equation (8)). For $Ro < 2.35Ro_c$, the amplitude of the non-axisymmetric velocity, relative to U_0, increases with the forcing (figure 8(b)). After reaching a maximum, at $Ro = 2.35Ro_c$, the non-axisymmetric flow undergoes a decrease of its magnitude. Here the “efficiency” of the forcing to drive the non-zonal velocity is reduced as the Rossby waves smooth the gradient of vorticity and so affect their excitation mechanism.

The back reaction on the forcing velocity in the upper molecular hydrogen layer is not taken into account in our model although it might significantly affect the zonal profile in the case of strong forcing.

3.2.2 Model N

The shear instability takes the form of an $m = 2$ oscillation in the azimuthal direction (figure 9). It is a single wave propagating eastward with the same frequency over the shell, and it is nearly z-invariant. The maxima of the non-zonal vorticity are located on each side of the prograde jet. The characteristics of this wave are similar to the Rossby wave obtained with the model J. The frequency of this wave is in agreement with the frequency of the theoretical Rossby wave of wavenumber $m = 2$ propagating at a radius $s = 0.53$ (assuming that $k_s \approx m/s$ in the dispersion relation (6)). Using the instability criterion (8) with the geostrophic profile we obtain a critical Rossby number of 0.026 in good agreement with the numerical results when the Ekman number decreases (detailed in A).

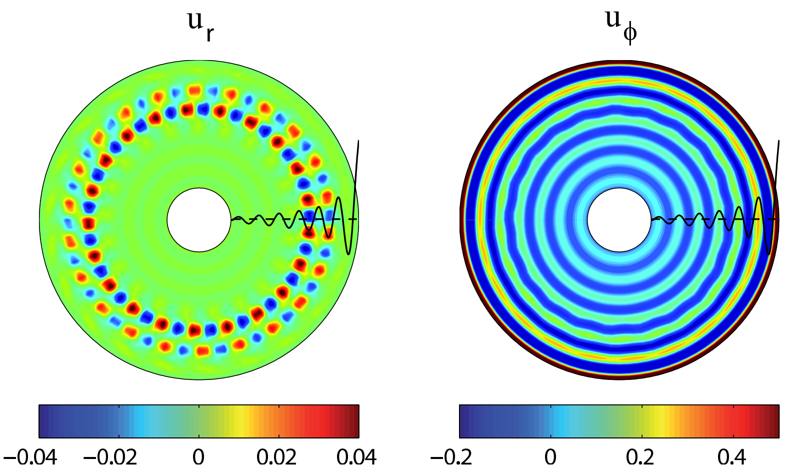

(a) $Ro = 1.06 Ro_c$

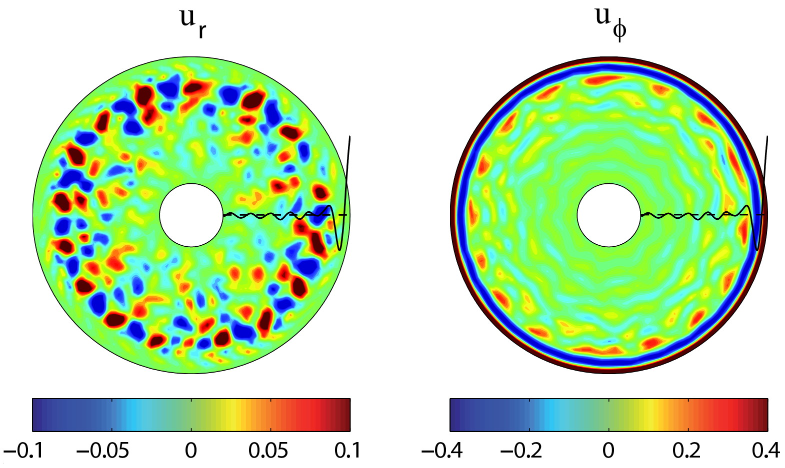

(b) $Ro = 2.94 Ro_c$

Figure 7: Snapshots of the radial (left) and azimuthal (right) velocity components in the equatorial plane for $E = 5 \times 10^{-6}$ and $Ro > Ro_c$ for the model J. The velocities are scaled by U_0. For u_ϕ the colorscale has been truncated $(u_\phi(r_o, \theta = \pi/2, \phi) = 1)$.

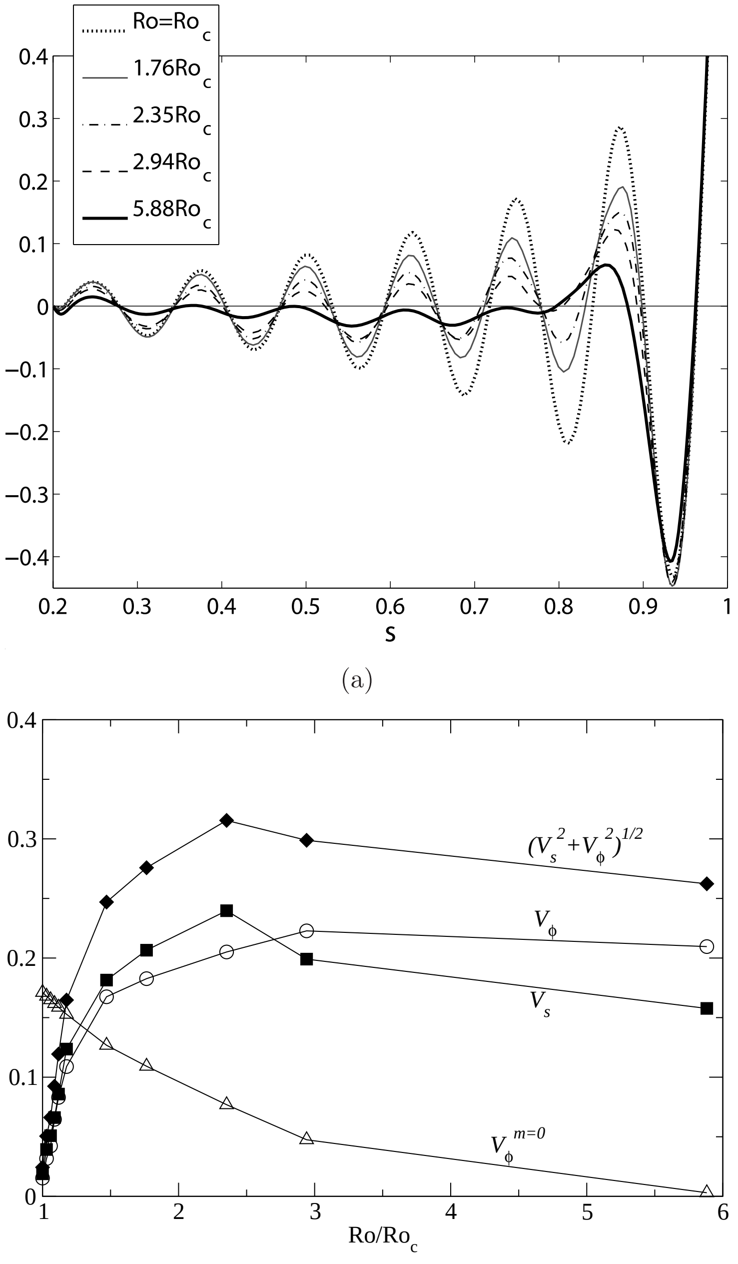

(a)

(b)

Figure 8: (a) Time-averaged zonal velocity in the equatorial plane for $E = 5\times10^{-6}$ and different forcings. (b) Amplitude of the non-axisymmetric radial velocity V_s (squares), the non-axisymmetric azimuthal velocity V_ϕ (circles), the amplitude of non-axisymmetric velocity $(V_s^2 + V_\phi^2)^{1/2}$ (diamonds) and the zonal velocity at the radius $s = 0.75$ (triangles). All velocities were measured in the equatorial plane in the units of U_0. The amplitude of the non-axisymmetric velocity corresponds to the maximum in a snapshot, whereas the zonal velocity amplitude has been averaged in time.

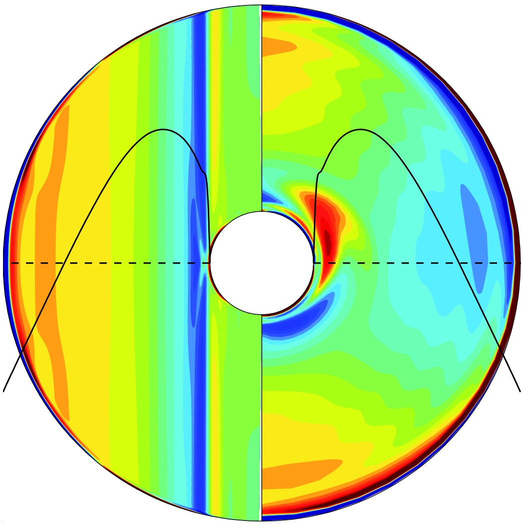

Figure 9: Non-zonal axial vorticity in the equatorial plane (right) and in a meridional slice (left) for the model N at $E = 5 \times 10^{-6}$ and $Ro = 1.01Ro_c$ (blue: negative and red: positive). The black line represents the zonal velocity in the equatorial plane.

4 Magnetic field generation

The non-axisymmetric motions are of prime importance for the dynamo mechanism because a purely toroidal flow cannot generate a self-sustained magnetic field. We note that some axisymmetric poloidal flow is present when $Ro < Ro_c$ as a weak meridional circulation is created by the Ekman pumping. However these motions are weak at small Ekman numbers so we do not expect to find dynamos when the zonal flow is stable, that is when $Ro < Ro_c$, in the asymptotic inviscid regime. Indeed we did not find dynamos when $Ro < Ro_c$ (up to $Pm = 10$). The non-axisymmetry associated with the hydrodynamic shear instability is a crucial element for the dynamo process: the stable zonal flow cannot sustain a magnetic field by itself. This is in agreement with the results obtained by Guervilly and Cardin (2010) with dynamos generated by spherical Couette flows (differential rotation between two concentric spheres).

4.1 Characteristics of the magnetic field for the model J

We have performed dynamo simulations for $Ro = 1.17 - 1.76Ro_c$ and $E = 5 \times 10^{-6}$. We find that the dynamo threshold occurs at a rather high value of the magnetic Prandtl number, $Pm_c \approx 5$. The critical magnetic Reynolds number (defined via the maximum forcing velocity) required for dynamo action is $Rm_c \approx 20000$ (see the conclusion section for an estimate of the critical magnetic Reynolds number defined via the local velocity). For a given forcing, we have performed calculations just above the critical magnetic Prandtl number, Pm_c, and up to $2Pm_c$.

The main features of the self sustained magnetic field can be observed in figures 10 and 11. The magnetic field displays a dipolar symmetry, *i.e.* antisymmetry with respect to the equatorial plane,

$$(B_r, B_\theta, B_\phi)(r, \pi - \theta, \phi) = (-B_r, B_\theta, -B_\phi)(r, \theta, \phi). \tag{10}$$

The magnetic field is predominantly toroidal and axisymmetric (corresponding to the mode $m = 0$ in figure 11(a)). The toroidal magnetic field does not emerge from the conducting region as the outer region is electrically insulating. The strongest poloidal component is the axial dipole within the conducting region and outside of the outer sphere (corresponding to the harmonic $(l, m) = (1, 0)$ in figure 11). The field lines of the axisymmetric poloidal field are bent in the region of propagation of the Rossby wave where a strong induction of magnetic field occurs (figure 10(a)). A magnetic field at the scale of the Rossby wave is produced in this region as can be observed on the spectra of magnetic energy (figure 11(a)) with significant peaks at $m = 22$ in the poloidal and toroidal magnetic energies and at $l = 23$ in the poloidal magnetic energy ($l - m$ is odd to preserve the dipolar symmetry). Close to the outer boundary, the axisymmetric poloidal magnetic field lines converge and diverge locally (figure 10(a)). This is due to the induction of axisymmetric magnetic field by the secondary meridional circulation produced by Ekman pumping. This effect is very localised and generates a magnetic field of small latitudinal scale that decreases rapidly with radius.

The spectrum and map of the radial magnetic field at the surface of our modelled planet (at radius $r_s = 1.25r_o$) (figures 10(b) and 11(b)) show that the magnetic field is strongly dominated by the axial dipole and the axisymmetric mode. The magnetic field generated at the scale of the Rossby wave ($m = 22$) is still visible in the spectrum of the magnetic field but its amplitude is weak at this radius: about 4 orders of magnitude smaller than the amplitude of the axisymmetric mode (note that the spectrum in figure 11(b) represents the squared amplitude of the field).

In all the simulations performed, no inversion of polarity of the axial dipole has been observed. The tilt of the dipole is rather weak, at most 2° from the rotation axis (figure 12). We found a secular variation of the dipole axis (about 1° every 1000 rotation periods). Note that our simulations

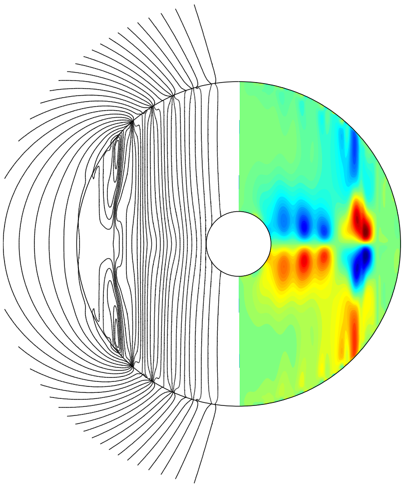

(a) Axisymmetric magnetic field

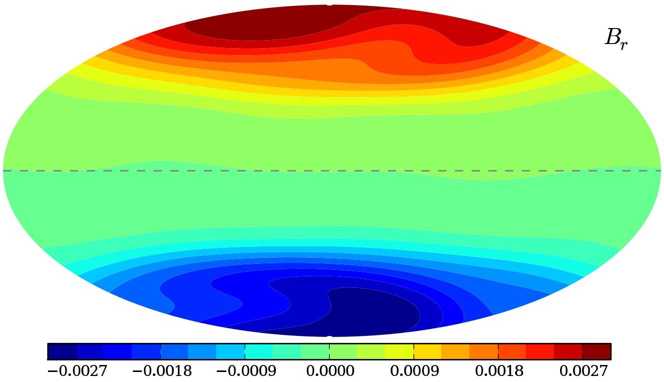

(b) Radial magnetic field at r_s

Figure 10: Magnetic field for model J. (a) Snapshot of the axisymmetric magnetic field in a meridional plane: magnetic poloidal field lines (left) and azimuthal magnetic field (coloured, right) (red: positive, blue: negative). (b) Map of the radial magnetic field at the surface of the planet $r_s = 1.25 r_o$ in unit of $\sqrt{\rho\mu_0}U_0$ The poloidal magnetic field at $r = r_s$ is calculated assuming

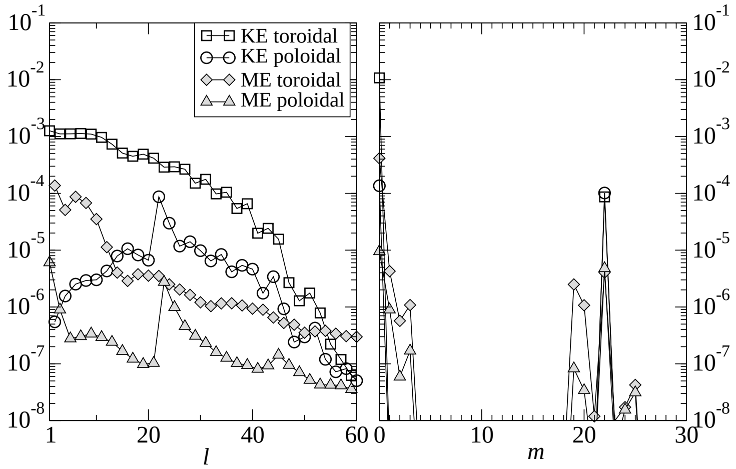

(a) Kinetic and magnetic energies in the fluid

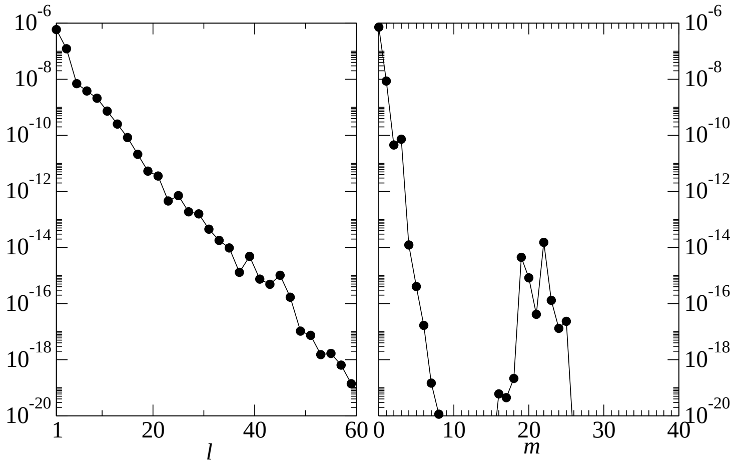

(b) A_l and A_m at r_s

Figure 11: Magnetic energy spectra for model J. (a): Kinetic (KE) and magnetic (ME) energy per unit volume for each spherical harmonics degree l (left) and mode m (right) in the fluid conducting region given in unit of ρU_0^2. (b): Squared amplitudes of the magnetic field, A_l (left) and A_m (right) as defined in figure 2, at $r_s = 1.25 r_o$ given in unit of $\rho \mu_0 U_0^2$. Only the degrees of significant amplitude have been plotted, that is, l even for the kinetic poloidal and magnetic toroidal energies and l odd for the kinetic toroidal and magnetic poloidal energies. These data are taken at a particular instant and have not been time-averaged. Same parameters than figure 10.

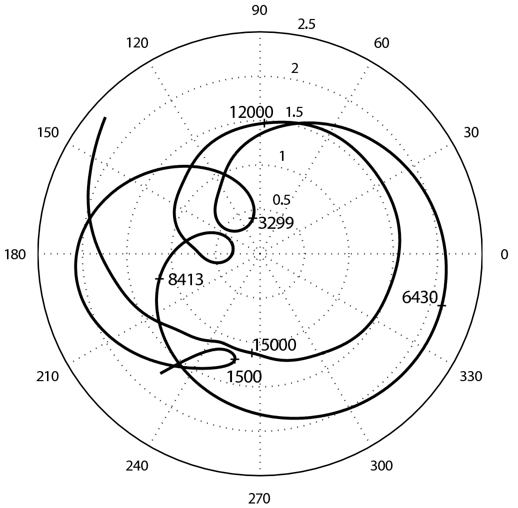

Figure 12: Drift of the dipole axis with time in a polar representation. The tilt of the dipole axis λ is calculated with the formula $\lambda = \tan^{-1}\left[((g_1^1)^2 + (h_1^1)^2)^{1/2}/g_1^0\right]$ with g_m^l and h_m^l the Gauss coefficients of degree l and order m. The longitude of the dipole axis is $\beta = \tan^{-1}\left(-h_1^1/g_1^1\right)$. On the polar representation, the tilt is the deviation of the dipole axis from the rotation axis in degree. The annotations on the curve indicate the time in rotation periods. Same parameters than figure 10.

are performed for dynamos slightly critical and their time-dependence may increase for higher Pm.

Just above the dynamo threshold ($Pm_c < Pm \leqslant 2Pm_c$), the magnetic field is weak: the magnetic energy contained within the fluid conducting region is only about 5% of the kinetic energy. The magnetic field does not strongly act back on the flow, except to produce its own saturation. A comparison between the zonal flow in the non-magnetic case and in the presence of the dynamo magnetic field does not reveal significant differences. The magnetic field lines of the poloidal field are almost aligned with the rotation axis and the flow structure (see figure 10(a)). Consequently for a stronger magnetic field (at larger magnetic Reynolds numbers) with the same geometry, the flow disruption due to the Lorentz forces would still be weak.

4.2 Characteristics of the magnetic field for the model N

We performed simulations at $Ro = 1.05 - 1.5Ro_c$ and $E = 10^{-5}$. We find the dynamo threshold at $Pm_c \approx 1$, that is, the critical magnetic Reynolds number is $Rm_c \approx 4000$.

The main features of the self sustained magnetic field can be observed on figures 13 and 14. The self-sustained magnetic field displays an equatorial symmetry, *i.e.*

$$(B_r, B_\theta, B_\phi)(r, \pi - \theta, \phi) = (B_r, -B_\theta, B_\phi)(r, \theta, \phi). \tag{11}$$

Within the fluid conducting region, the axisymmetric toroidal field is the strongest component whereas the poloidal field is dominated by the $m = 2$ mode, not the axisymmetric $m = 0$ mode. The $m = 2$ mode corresponds to the magnetic field generated at the scale of the Rossby wave (figure 14(a)). The axisymmetric poloidal field is multipolar, mainly composed by an axial quadrupole ($(l, m) = (2, 0)$) and the $(l, m) = (4, 0)$ mode. At the surface of the planet (figure 14(b)), the magnetic field appears to be mainly axisymmetric (with the $l = 2$ and $l = 4$ harmonics degrees dominant) but the $m = 2$ structure is still of significant amplitude, about 2 orders of magnitude smaller than the $m = 0$ mode and visible at high latitudes on the map of the radial field at the surface (dark blue patches in figure 13(b)).

Due to the equatorial symmetry of the field, the magnetic field lines in the equatorial plane are roughly perpendicular to the cylindrical structure of the flow whereas they are nearly aligned at higher latitudes (figure 13(a)). As a result magnetic braking acting on the flow is stronger in the equatorial region than at high latitude regions. In the simulation performed here ($Pm_c < Pm \leqslant 2Pm_c$), the magnetic energy is weak compared to the kinetic energy (about 5%) so the feedback of the magnetic field on the flow remains weak. For a stronger magnetic field (at larger magnetic Reynolds numbers), we expect that the flow disruption would become important. As a result the equatorially symmetric solution may become unstable and the magnetic field may switch to an axial dipolar symmetry. This is the result obtained by Aubert and Wicht (2004) in convectively-driven dynamos: they found equatorial dipolar magnetic fields for Rayleigh numbers close to the convection onset; these solutions become unstable as the convective forcing is increased and an axial dipolar configuration is preferred.

In summary, the flows driven by the profiles J and N produce very different poloidal magnetic fields: mainly a strongly axisymmetric dipole for the profile J and a weak multipolar axisymmetric field dominated by the magnetic field induced at the scale of the Rossby waves for the profile N. In both cases the magnetic field within the conducting region is mainly an axisymmetric toroidal field. The different magnetic field morphology is quite surprising given that the flows are quite similar : strong zonal flows and propagating Rossby waves. In the next section we review the dynamo mechanism that

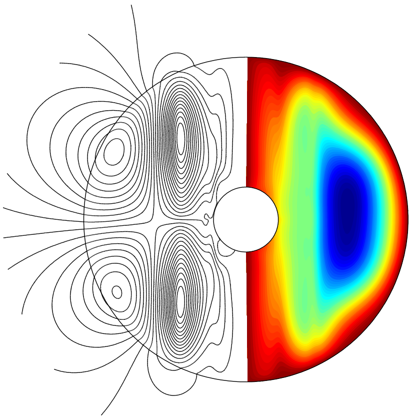

(a) Axisymmetric magnetic field

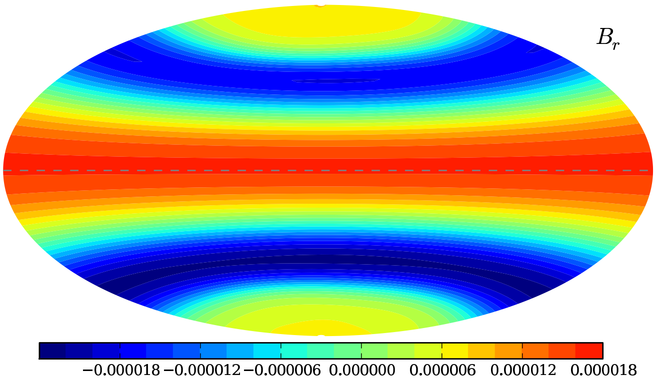

(b) Radial magnetic field at r_s

Figure 13: Magnetic field for model N (same as figure 10). For the axisymmetric azimuthal field, blue corresponds to negative values and red to zero values. The radial magnetic field is plotted at the surface of the planet $r_s = 1.18r_o$. The parameters of this simulation are $E = 10^{-5}$, $Ro = 1.20Ro_c$ and $Pm = 2 \approx 2Pm_c$.

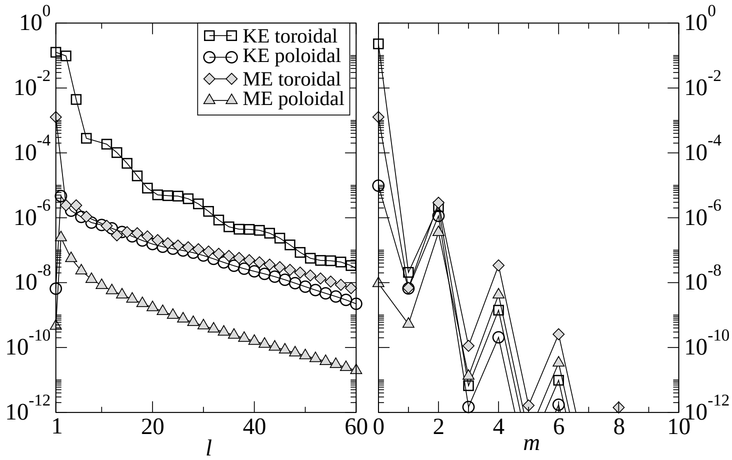

(a) Kinetic and magnetic energies in the fluid

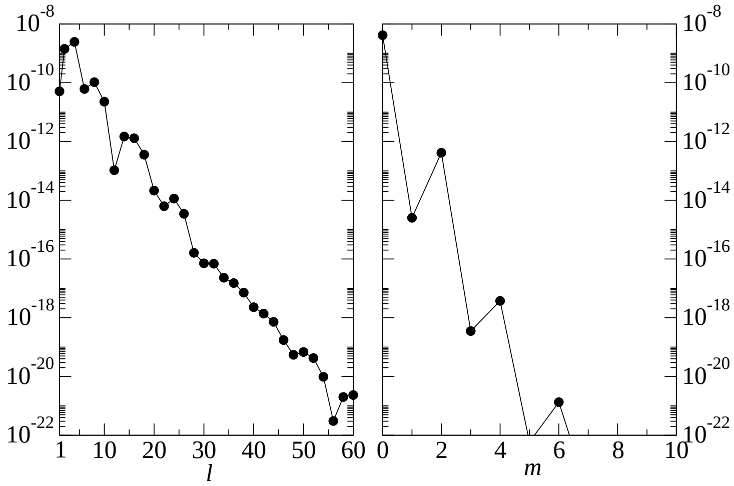

(b) A_l and A_m at r_s

Figure 14: Magnetic energy spectra for model N (same as figure 11). Only the degrees of significant amplitude have been plotted, that is, l even for the kinetic poloidal and magnetic poloidal energies (plus $l = 1$) and l odd for the kinetic toroidal and magnetic toroidal energies. Same parameters than figure 13.

has been proposed to operate for similar flows and suggest the key difference between profiles J and N that determines the topology of their self-sustained magnetic fields.

4.3 Dynamo mechanism

Using a quasi-geostrophic flow and a kinematic approach (no Lorentz force in the momentum equation), Schaeffer and Cardin (2006, hereafter SC06) obtain numerical dynamos generated by an unstable Stewartson layer: for a strong enough forcing, the Stewartson layer is unstable to non-axisymmetric shear instabilities, which appear in the form of Rossby waves (of wavenumber about 10 for the Ekman numbers and Rossby numbers they investigated). The self-sustained magnetic field displays a strong axisymmetric toroidal magnetic field and a mostly axisymmetric poloidal field. SC06 show that the time dependence of the flow is a key ingredient for the dynamo effect: time-stepping the magnetic induction equation using a steady flow taken either from a snapshot or a time-average leads to the decay of the magnetic field. They characterize the dynamo process as an $\alpha\omega$ mechanism. In mean field theory, the α effect requires that the flow possess some helicity, the correlation between fluid velocity and vorticity, $H = \mathbf{u} \cdot \boldsymbol{\omega}$ (*e.g.* Moffatt, 1978). Flows displaying a columnar structure aligned with the axis of rotation, such as Rossby waves or convection columns (Olson et al., 1999), typically possess strong mean helicity. As these columns are essentially bidimensional vortical structures, the helicity is mainly produced by the term $u_z \omega_z$. In nearly z-invariant flow, the axial (z) velocity is mostly due to two terms: the slope effect and the Ekman pumping. The slope effect comes from the combination of mass conservation and impenetrable boundaries: a (cylindrical) radial velocity u_s creates an axial velocity $u_z \sim z\beta u_s$ with $\beta = h^{-1}(dh/ds)$. In the limit of rapid rotation in a spherical container, this contribution is much larger (of order 1) than the Ekman pumping ($u_z \sim E^{1/2}\omega_z$). However, the axial velocity produced by the slope effect is phase shifted by $\pi/2$ with ω_z, and so does not allow the production of mean helicity. On the contrary, axial velocity produced by Ekman pumping is in phase with the axial vorticity and a dynamo mechanism based on the Ekman pumping associated to an azimuthal necklace of axial vortices is plausible (Busse, 1975). In a numerical experiment at small Ekman numbers ($E = \mathcal{O}(10^{-8})$), SC06 artificially remove the Ekman pumping and observe dynamo action with nearly the same threshold showing that the Ekman pumping is unimportant in their dynamo mechanism. The crucial importance of the time dependence of the flow and the negligible contribution of the Ekman pumping lead SC06 to consider the involvement of the Rossby waves in the dynamo process. In mean field theory, an axisymmetric poloidal magnetic field is produced from the correlation of small scale magnetic field and velocity (α effect). SC06 suggest that a "giant α effect" may be associated with the Rossby waves. They conjecture that the propagation of the Rossby waves yields a phase shift between the non-axisymmetric magnetic field and velocity field in order to produce the axisymmetric poloidal magnetic field.

Avalos-Zuniga et al. (2009) have calculated the α tensor, describing the generation of a large scale magnetic field by correlation of small scale velocity and magnetic field, with a flow geometry corresponding to Rossby waves. In the absence of Ekman pumping, they show that the diagonal components of the α tensor, which are the relevant coefficients for the α effect, are non-zero if and only if the flow pattern is drifting relative to the mean flow.

Tilgner (2008) explains that the time dependence of a velocity field can lead to dynamo action even when any particular snapshot of the velocity field cannot because the linear operator associated with the induction equation is non-normal. In particular, he shows that the simple time dependence of a propagating wave is enough for dynamo action. Several numerical studies report the importance of the time dependence of the velocity field, mainly of oscillating nature (Reuter et al., 2009; Gubbins, 2008).

The idea that the propagation of Rossby waves may maintain a dynamo action is very appealing as their presence is ubiquitous in rotating fluid dynamics. A system in which no wave propagation occurs, and which is unable to produce u_z by another mechanism, such as buoyancy, will rely on Ekman pumping to create axial velocity with the proper phase shift. However, in the limit of small Ekman number, the Ekman pumping vanishes and the dynamo threshold should become infinitely high. The dynamo mechanism relying on the propagation of Rossby waves is robust in the limit of small Ekman number as the presence of these waves does not rely on the action of viscosity.

Due to the close resemblance of the flow (zonal motions and propagating Rossby wave) in our 3D numerical model and the kinematic quasi-geostrophic model of SC06, we now try to establish if the dynamo mechanism described in SC06 is at work in our 3D model.

Let us first consider a simple theoretical model. The velocity field is composed by a zonal flow, $\overline{U}(s)\mathbf{e}_\phi$, and the small scale velocity of a Rossby wave $\mathbf{u}^m$ with

$$\mathbf{u}^m(s,\phi,z,t) = (u_s^m(s,z)\mathbf{e_s} + u_\phi^m(s,z)\mathbf{e}_\phi + u_z^m(s,z)\mathbf{e_z})\exp(i(m\phi-\omega t)) \quad (12)$$

where u_s^m, u_ϕ^m and u_z^m are complex and ω is the frequency of the wave. The magnetic field is composed of an axisymmetric magnetic field $\overline{\mathbf{B}}$, and a magnetic field perturbation induced at the scale of the Rossby wave $\mathbf{b}^m$ with

$$\mathbf{b}^m(s,\phi,z,t) = (b_s^m(s,z)\mathbf{e_s} + b_\phi^m(s,z)\mathbf{e}_\phi + b_z^m(s,z)\mathbf{e_z})\exp(i(m\phi-\omega t)+\lambda t) \quad (13)$$

where b_s^m, b_ϕ^m and b_z^m are complex and λ is the growth rate of the magnetic field. The equations for the evolution of the poloidal components of $\overline{\mathbf{B}}$ in cylindrical coordinates $\overline{B_s}$ and $\overline{B_z}$ are

$$\begin{aligned}
\frac{\partial \overline{B_s}}{\partial t} &= -\frac{\partial}{\partial z}\left(\overline{u_z^m b_s^m - u_s^m b_z^m}\right) + \eta\left(\nabla^2 \overline{B_s} - \frac{\overline{B_s}}{s^2}\right), && (14)\\
\frac{\partial \overline{B_z}}{\partial t} &= \frac{1}{s}\frac{\partial}{\partial s} s\left(\overline{u_z^m b_s^m - u_s^m b_z^m}\right) + \eta\nabla^2 \overline{B_z}, && (15)
\end{aligned}$$

where the overbar denotes an azimuthal average. It is immediately apparent that if u_s^m (u_z^m) is out of phase by $\pi/2$ with b_z^m (resp. b_s^m), then $\overline{B_s}$ and $\overline{B_z}$ will be decaying in time. If we suppose that $\overline{B_\phi} \gg \overline{B_s}, \overline{B_z}$ the equations for b_s^m and b_z^m are

$$\begin{aligned}
(\lambda - ic\frac{m}{s})b_s^m &= \frac{im}{s}u_s^m\overline{B_\phi} + \eta\left(\nabla^2 b_s^m - \frac{2}{s^2}\frac{\partial b_\phi^m}{\partial \phi} - \frac{b_s^m}{s^2}\right), && (16)\\
(\lambda - ic\frac{m}{s})b_z^m &= \frac{im}{s}u_z^m\overline{B_\phi} + \eta\nabla^2 b_z^m. && (17)
\end{aligned}$$

where $c = (\omega/(m/s) - \overline{U})$ is the phase speed of the wave relative to the mean flow $\overline{U}$. In the case of marginal stability ($\lambda = 0$), if we neglect the magnetic diffusivity η then we obtain that b_s^m (b_z^m) is in phase with u_s^m (u_z^m resp.). Moreover if the axial velocity is mainly due to the slope effect then $u_z^m = z\beta u_s^m$ and so according to the equations (16)-(17) $b_z^m \approx z\beta b_s^m$. This implies that the first term of the right hand side of equations (14)-(15) is almost zero and thus $\overline{B_s}$ and $\overline{B_z}$ are decaying. Consequently magnetic diffusivity must play a role in the generation of the axisymmetric poloidal magnetic field. Note that the importance of magnetic diffusivity is well established in the α effect (Roberts, 2007). On the other hand, if the wave is not propagating, $c = 0$, then

$$\begin{aligned}
-\frac{im}{s}u_s^m\overline{B_\phi} &= \eta\left(\nabla^2 b_s^m - \frac{2}{s^2}\frac{\partial b_\phi^m}{\partial \phi} - \frac{b_s^m}{s^2}\right), && (18)\\
-\frac{im}{s}u_z^m\overline{B_\phi} &= \eta\nabla^2 b_z^m. && (19)
\end{aligned}$$

In this case the magnetic field perturbations b_s^m and b_z^m are out of phase with u_s^m and u_z^m (as u_s^m and u_z^m are correlated by the slope effect) and so the averaged products $\overline{u_z^m b_s^m}$ and $\overline{u_s^m b_z^m}$ are zero. We can conclude that in

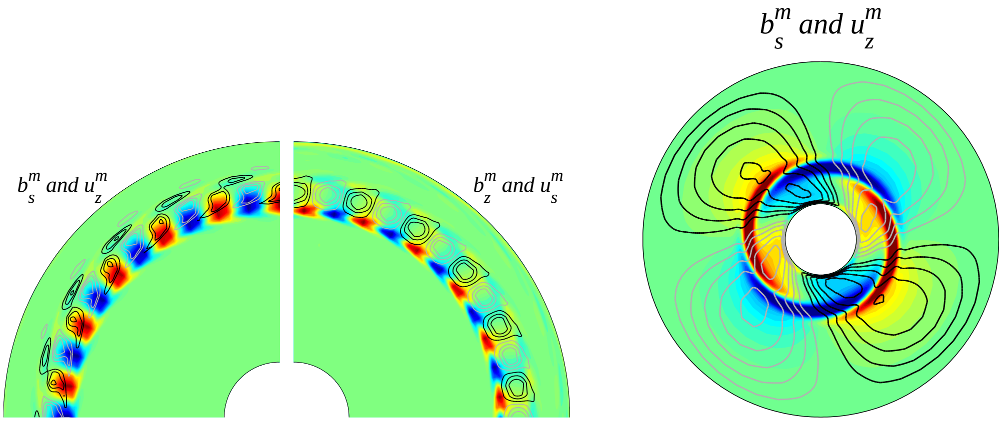

(a) Model J (b) Model N

Figure 15: Non-axisymmetric radial magnetic field (colour) and non-axisymmetric radial velocity (black lines: positive, and gray lines: negative): (a) for the model J in a quarter of a plane a few degree of latitude above the equatorial plane (northern hemisphere) and (b) for the model N in the equatorial plane. Same parameters than figures 10 and 13.

order for this simple model to work as a mean-field dynamo (i) the wave must propagate and (ii) the magnetic diffusivity must act on the magnetic field generated at the scale of the waves. As the Rossby wave propagates, the location of the induction of the magnetic field perturbation is forced to drift with the same rate, but with a phase-shift. The phase-shift between the magnetic field perturbation and the Rossby wave depends on both the phase speed c and the magnetic diffusivity η. The argument above implies that this phase-shift is essential for the dynamo mechanism.

Using any particular snapshot of the velocity field for the time stepping of the magnetic induction in our numerical simulations with the models J or N yields the decay of the magnetic field. The failure of dynamo in the kinematic numerical experiment is readily explained by our simple theoretical model.

In figure 15(a), we plot the non-axisymmetric components of the velocity, u_z^m and u_s^m and magnetic field, b_s^m and b_z^m obtained in the numerical simulations for the model J in a plane located just above the equatorial plane (b_s^m and b_z^m are zero in the equatorial plane by dipolar symmetry). All the non-axisymmetric components are plotted but clearly $m = 22$ is dominant. The correlation of u_z^m with u_s^m confirms that u_z^m is mainly produced by the slope effect. We observe that u_z^m and b_s^m are in phase so $\overline{u_z^m b_s^m}$ has a significant amplitude in the equations (14)-(15). b_z^m is however out of phase with u_s^m, which means that $\overline{u_z^m b_s^m} \gg \overline{u_s^m b_z^m}$. This may be an effect of the magnetic diffusivity as b_s^m and b_z^m have different spatial structures, or due to radial derivatives of $\overline{B_s}$ and $\overline{B_z}$ that we neglect in equation (17).

In figure 15(b) we plot the non-axisymmetric radial magnetic field, b_s^m, together with the non-zonal radial velocity, u_s^m for the model N. Strong positive (negative) crescent-shaped patches of b_s^m are visible in the cyclonic (resp. anticyclonic) vortices (out of phase by $\pi/2$ with u_s^m). Round-shaped lobes of b_s^m of weaker amplitude are observed in phase with u_s^m. The axial velocity u_z^m is in phase with the radial velocity u_s^m (not shown) and again is mainly due to the slope effect. The axial magnetic field b_z^m is in phase with b_s^m (not shown). Consequently the strongest amplitudes of b_s^m and b_z^m (crescent-shape) do not participate to the term $\overline{u_z^m b_s^m}$ and $\overline{u_s^m b_z^m}$. These maxima of b_s^m are out of phase with u_s^m in contradiction with the theoretical model (equations (16) and (17)). This non-axisymmetric magnetic field is thus mainly created by a mechanism that is not described by our simplified model such as the axial and radial derivatives of $\overline{B_s}$ and $\overline{B_z}$, which are important in this region (see figure 13(a)). The magnetic field b_s^m of small amplitude (round-shaped lobes) in phase with u_s^m maintains a weak axisymmetric multipolar magnetic field compared with the $m = 2$ component. At the surface of the planet this axisymmetric field is the dominant component but in comparison with the strongly axisymmetric dipolar field produced with the model J, the field appears to be of small amplitude: at $Rm = 1.17Rm_c$ ($Ro = 1.17Ro_c$ and $Pm \approx Pm_c$) the amplitude of the axisymmetric radial field is about $10^{-3}\sqrt{\rho\mu_0}U_0$ for the model J (figure 11(b)) while it is only $10^{-4}\sqrt{\rho\mu_0}U_0$ for the model N at $Rm_c = 2.4Rm_c$ ($Ro = 1.20Ro_c$ and $Pm = 2Pm_c$) (figure 14(b)).

The main difference between the Rossby waves of the models J and N is their size. The phase speed of the Rossby wave, $c \approx \Omega\beta/(m/s)^2$, increases when its wavenumber decreases: for a fixed radius s and rotation rate Ω, a $m = 2$ Rossby wave (as obtained with the model N) propagates with a phase speed about 100 times faster than a $m = 22$ wave (as obtained with the model J). If the wave is too fast, the typical timescale of magnetic diffusion at the scale of the vortex is long in comparison of the period of the wave. The typical propagation timescale for a Rossby wave of size d is $\tau_{rw} = 1/(\Omega\beta d)$ assuming that the radial and azimuthal lenghtscales of the wave are similar. The magnetic diffusion timescale at the scale of the vortex d is $\tau_\eta = d^2/\eta$. The ratio of the two timescales is

$$\frac{\tau_\eta}{\tau_{rw}} = \frac{d^3\Omega\beta}{\eta}. \tag{20}$$

The dependence to the third power of the size, $d \propto 1/m$, shows that the magnetic diffusion acting on a $m = 22$ wave is about 3 orders of magnitude larger than on an $m = 2$ wave for the same parameter values. For the simulation presented for the model N, the ratio τ_η/τ_{rw} is about 10^5. Note that for the model J the ratio τ_η/τ_{rw} is about 500 so the propagation of the Rossby wave is still much more rapid than the magnetic diffusion. For both models, we found that the values of the small scale magnetic field in phase with the velocity is of the same order of magnitude. The velocity field of the vortices is also about the same order of magnitude for the two models. However as b_s^m and b_z^m are in phase in the model N due to the very slow action of magnetic diffusion on the $m = 2$ magnetic structures, the terms $\overline{u_s^m b_z^m}$ and $\overline{u_z^m b_s^m}$ tend to cancel out. The very slow diffusion of the magnetic field compared with the fast propagation of the $m = 2$ Rossby wave therefore leads to very little generation of axisymmetric poloidal magnetic field.

The last stage of the dynamo mechanism is the generation of the axisymmetric toroidal field. It can either be produced from the correlation of small scale velocity and magnetic field (as an α effect) or an ω effect, that is the shearing of the axisymmetric poloidal magnetic field by the mean zonal flow $\overline{U}$. SC06 find that the ω effect from the Stewartson layer is dominant in their numerical model. The zonal shear produced in the Stewartson layer is stronger than the shear we obtained with the profiles J and N, so it is not clear that the ω effect is important in our model *prima facie*. In α^2 dynamos, both toroidal and poloidal components are typically of similar magnitudes (Olson et al., 1999). Here, the strong toroidal magnetic field suggests that the ω effect is more important. To confirm this, we plot in figure 16 the term responsible for the ω effect in the azimuthal component of the magnetic induction equation (Gubbins and Roberts, 1987), $r\overline{B_r}\partial_r(r^{-1}\overline{U}) + r^{-1}\sin\theta\overline{B_\theta}\partial_\theta(\sin\theta^{-1}\overline{U})$. For the model J, as we expect, this term is most significant in the region where the poloidal magnetic field lines are bent and misaligned with the zonal flow structure, that is, in the region where the Rossby wave propagates (see figure 10(a)). The correlation of sign and location of the maxima of the ω effect in the bulk of the fluid with the axisymmetric azimuthal field indicates that it is mainly generated by the ω effect. Note that some ω effect is also present close to the outer boundary, where the poloidal magnetic field lines converge and diverge locally due to induction by the Ekman pumping. However no particularly strong axisymmetric azimuthal magnetic field is produced in this region (figure 10(a)) so this small scale field diffuses probably very rapidly. For the model N the outer part of the jet ($s > 0.5$) is retrograde and creates a negative ω effect whose sign and location correlate with the axisymmetric azimuthal field, implying that the main dynamo process in the outer region is indeed the ω effect. However, $\overline{B_\phi}$ and the ω effect are anti-correlated in the inner region ($s < 0.5$) so another dynamo process such as a correlation of small scale

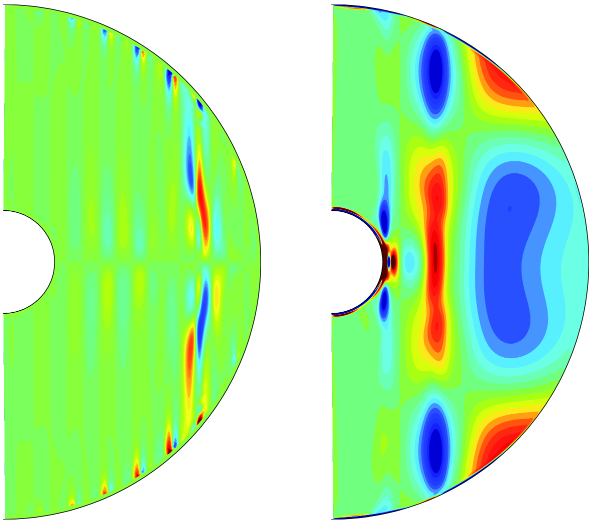
(a) Model J (b) Model N

Figure 16: ω effect in the meridional plane in the bulk (outside the Ekman layers) (red: positive, blue: negative). Same parameters than figures 10 and 13.

velocity and magnetic field must be at work there.

We have not yet addressed the question of the selection of the axial dipolar symmetry (equation 10) or the axial quadrupolar symmetry (equation 11). In kinematic dynamo calculations, Gubbins et al. (2000) show that minor changes in the flow can select very different eigenvectors. For a self-consistent system the selection rules are thus very subtle. As discussed in section 4.2, Aubert and Wicht (2004) found that axial quadrupolar symmetry is incompatible with the vertical structures of cyclones and anticyclones in convectively-driven dynamos, and so these solutions are unstable for strong convective flows. In our simulations of the model N, this conclusion suggests that the axial quadrupolar symmetry would be unstable for larger magnetic Reynolds numbers, and an axial dipolar field would be preferred. The selection of a given symmetry does not modify our argument that the wavenumber of the Rossby mode determines the amplitude of the axisymmetric magnetic field since no particular latitudinal symmetry is assumed.

In this study, it appears that the dynamo mechanism relies on a subtle balance between the Rossby wave propagation and the magnetic diffusion and therefore is closely related to the size of the Rossby waves. The dynamo field produced with this mechanism requires high magnetic Reynolds numbers ($Rm_c \approx 20000$ for the model J and $Rm_c \approx 4000$ for the model N). However, in the limit of small Ekman numbers, this dynamo mechanism is expected to keep a finite value of the critical magnetic Reynolds number (Schaeffer and Cardin, 2006), whereas dynamos relying on Ekman pumping should occur at a threshold that becomes infinitely high.

5 Conclusions

We numerically studied the dynamics of zonal flows driven by differential rotation imposed at the top of a conducting layer and how they sustain a magnetic field.

5.1 Hydrodynamical instability

In our hydrodynamical simulations, we found that the destabilisation of the zonal flow takes the form of a global (large radial extension) Rossby mode, even though the instability threshold is governed by a local criterion. The wavenumber depends on the width of the jets, and is independent of the viscosity and rotation rate providing the former is sufficiently small. In the supercritical regime, several Rossby waves appear and saturate the amplitude of the zonal flow in the bulk of the fluid. They produce a widening of the jets and a strong damping of their amplitude, even for relatively small supercritical forcing ($Ro = 2.94 Ro_c$).

5.2 Constraints on the dynamo mechanism

In the limit of small Ekman number, we find that the Rossby wave appears for $Ro_c \approx 0.001$ for a Jupiter-like zonal wind profile (model J) and $Ro_c \approx 0.02$ for a Neptune-like profile (model N). In our numerical calculations, non-axisymmetric motions are necessary for dynamo action to occur. As the viscosity is overestimated in the numerical simulations compared to the planetary values, the Reynolds number is much smaller in the simulations. To reach a sufficiently high magnetic Reynolds number, the magnetic Prandtl number is of order 1, much larger than the expected planetary values. The critical magnetic Reynolds number Rm_c is about 20000 for the model J and 4000 for the model N. To make this dynamo mechanism work, two constraints must be satisfied: (i) $Ro > Ro_c$ and (ii) $Rm > Rm_c$. Equivalently this gives constraints on the amplitude of the zonal motions at the top of the conducting region, $U_0 > Ro_c \Omega r_o$, and on the electrical conductivity within the conducting region, $\sigma > Rm_c/(U_0 r_o \mu_0)$.

The extrapolation of the constraint (i) to the giant planets is straightforward as the hydrodynamical instability threshold is independent of the

Ekman number, which is of order $10^{-15} - 10^{-16}$ for Jupiter (Guillot et al., 2004) and Neptune (Stevenson, 1983). For Jupiter ($r_o \approx 56,000$km and $\Omega = 1.8 \times 10^{-4}\text{s}^{-1}$), the equatorial velocity at the top of the conducting region, U_0, must be larger than 10m/s to have $Ro > Ro_c = 0.001$. For Neptune ($r_o \approx 21,000$km and $\Omega = 1.08 \times 10^{-4}\text{s}^{-1}$), U_0 must be larger than 45m/s to have $Ro > Ro_c = 0.02$. For both cases, this constraint is quite strong as it only allows for a factor 10 decrease of the amplitude of the zonal wind between the surface of the planet and the top of the deep conducting region, independently of the location of the top of this region.

The extrapolation of the constraint (ii) to the giant planets requires to know how the critical Reynolds number scales with the Ekman number. When varying the Ekman number from 10^{-6} down to 10^{-8}, Schaeffer and Cardin (2006) found that Rm_c remains constant (of the order of 10^4 in their simulations, close to the values found in our study). Based on their results, we assume that Rm_c is of the same order of magnitude when the Ekman number is close to the planetary values. For Jupiter, we obtain that the electrical conductivity should be larger than 30S/m to have $Rm > Rm_c = 20000$ (using $U_0 = 10$m/s). For Neptune, the electrical conductivity should be larger than 10S/m to have $Rm > Rm_c = 4000$ (using $U_0 = 45$m/s). This constraint on the conductivity is less restrictive than the constraint on the amplitude of the zonal motions and should be satisfied in the deep conducting layer of Jupiter (Nellis et al., 1999) and Neptune (Nellis et al., 1997).

We conclude that the differential rotation imposed by the zonal winds at the top of the conducting regions is a plausible candidate to drive the dynamo mechanism in the giant planets although a strong constraint on the amplitude of the zonal jet applies. Given the assumptions used in our model, such as incompressibility, constant conductivity, overestimate of the viscosity and viscous coupling between electrically insulating and conducting regions, this conclusion remains tentative. The robust nature of Rossby waves in the asymptotic limit of small Ekman numbers makes this dynamo mechanism seductive for planetary physical conditions.

5.3 Generation of the axisymmetric field and width of the jets

With a simple theoretical model, we show that the production of the axisymmetric field depends on the propagation of the Rossby waves and on the magnetic diffusion acting at the scale of the vortices. This model is in agreement with our numerical results: the magnetic diffusion rate of the $m = 2$ magnetic structures induced by the Rossby waves of the model N is nearly negligible compared to the propagation rate of the wave: as a result a weak axisymmetric poloidal magnetic field is generated; the magnetic diffusion acting on the $m = 22$ magnetic structures is not negligible compared to the propagation rate of the small size ($m = 22$) Rossby wave of the model J: a dominant axisymmetric poloidal magnetic field is generated. Consequently, in this model, the width of the zonal jets has an important influence on the generation of the axisymmetric magnetic field by controlling the size of the Rossby waves. Our results suggest that the difference in the magnetic fields and the surface zonal winds may be related if a (hydrodynamic or magnetohydrodynamic) mechanism can transport angular momentum between the surface and the deep, electrically conducting region.

The critical magnetic Reynolds number of this dynamo mechanism is large. However, in order to compare with other dynamos, a more significant number may be the critical local magnetic Reynolds number associated with magnetic induction by the Rossby wave velocity $Rm_c^l = V_s d/\eta$ where V_s is the typical non-zonal radial velocity and d is the lenghtscale of Rossby mode. For the dynamo obtained with the model J ($Rm_c = 20000$), $V_s \approx 0.1U_0$ and $m = 22$ so we find $Rm_c^l \approx 570$. For the dynamo obtained with the model N ($Rm_c = 4000$), $V_s \approx 0.01U_0$ and $m = 2$ so $Rm_c^l \approx 130$. Thus Rm_c^l is roughly $2 - 10$ times larger that the magnetic Reynolds number needed for dynamo action with a convective forcing (Christensen and Aubert, 2006).

5.4 Magnetic field at the planets' surface

With our numerical model, we obtain the presence of a peak at small azimuthal scale in the magnetic field spectrum that is correlated with the width of the hydrodynamically unstable zonal jets. This is an interesting observation as the magnetic measurements of forthcoming *Juno* mission (arrival at Jupiter in 2016) are expected to be of extraordinary quality due to the absence of a crustal magnetic field on Jupiter.

For the model J, we obtain a secular variation of the dipole tilt of about 1° in 3 years. The dipole is strongly axisymmetric with a tilt that does not exceed 2°. On Jupiter, the dipole axis tilt measured with the *Pioneer* and *Voyager* data compared with the *Galileo* measurements is larger (about 10°) and displays a secular variation of about 0.5° in 20 years (Russell et al., 2001). The strong axisymmetry of the dipolar field of the model J is in better agreement with the magnetic field of Saturn with a dipole tilt less than 1°(Russell and Dougherty, 2010).

5.5 Convective motions within the conducting region

In this work we have not taken into account the convective motions within the deep conducting region. Wicht et al. (2002) studied the linear stability of an imposed zonal flow in a spherical shell modelling the molecular hydrogen layer of Jupiter. They found that the critical Rossby number of the shear instability onset is almost independent of the Rayleigh number, which measures the strength of the convection. They concluded that the shear instability is only weakly modified by the presence of convection. On the other hand, they showed that the convection onset is strongly influenced by the presence of the zonal circulation, with the convection either enhanced or damped depending on the direction of the shear. However, their study is linear, and so the results cannot be extrapolated beyond the weakly non linear regime of convection. Whether or not our results apply in the presence of convection is a subject for future studies. In the presence of convection (which produces strong zonal motions and Rossby waves), and even for a convectively-driven dynamo (see for instance Aubert, 2005; Grote and Busse, 2001), the mechanism described here may still impose a similar relationship between the magnetic field morphology and the zonal wind profile.

Acknowledgements

Financial support was provided by the Programme National de Planétologie of CNRS/INSU. C.G. was supported by a research studentship from Université Joseph-Fourier Grenoble and by the U.S. Department of Energy - Office of Fusion Energy Sciences. The computations presented in this article were performed at the Service Commun de Calcul Intensif de l'Observatoire de Grenoble (SCCI) and at the Centre Informatique National de l'Enseignement Supérieur (CINES). We thank Jonathan Aurnou and the geodynamo group in Grenoble for useful discussions. The manuscript is submitted to Icarus and was substantially improved due to helpful suggestions by two anonymous referees.

A Onset of hydrodynamical instability and viscous effects

A.1 Model J

In this appendix we seek to determine whether the theoretical instability criterion (8) agrees with the instability obtained in the numerical simulations.

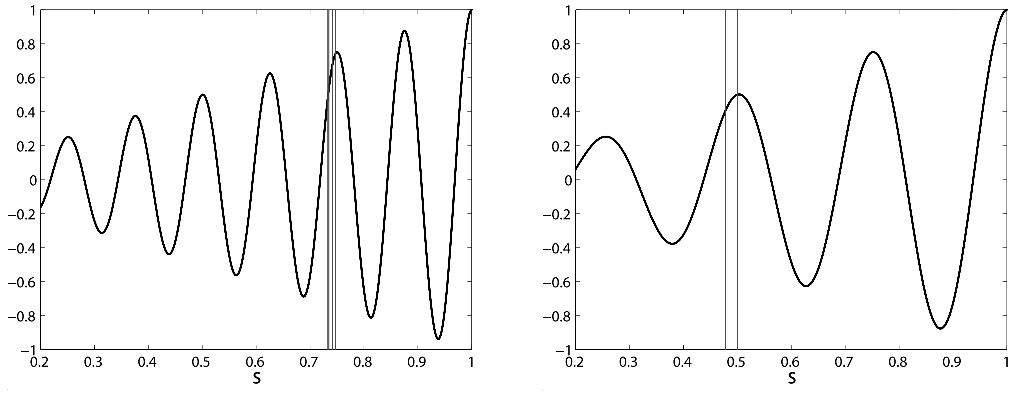

(a) Profile J

(b) Profile J2

Figure 1: Profile $U(s)$ in the equatorial plane (black bold line) and s_c (vertical lines) deduced from (6) using ω obtained from the simulations with $E = [5,4,3,2] \times 10^{-6}$ for the profile J and $E = [5,4] \times 10^{-6}$ for the profile J2.

In the numerical simulations the maximum of the non-zonal flow is always located within a retrograde jet (figure 6) whereas the barotropic instability is supposed to set in in a prograde jet in theory. To understand this apparent discrepancy ones has to bear in mind that the instability obtained in the numerical simulations displays a large radial extent (almost half of the gap), whereas the criterion (8) is local. If we suppose that the Rossby wave conserves the phase speed of the critical radius s_c given by the local criterion, then s_c can be inferred from the dispersion relation (6) and the frequency ω obtained in our simulations. In figure 1, we represent the profile U in the equatorial plane and s_c obtained for different E. s_c is close to the (fifth) prograde zonal jet. The jets being quite narrow, we check this observation by computing simulations using an imposed profile displaying wider jets. To do so we use $n_0 = 2$ in the formula (1) (see figure A.1(b), hereafter profile J2). For the profile J2, we also measure the frequency of the wave for different Ekman numbers. The results are presented on figure A.1(b) and back up the idea that s_c is located close to a maximum of zonal velocity, as predicted theoretically. Hence it appears that the onset of the instability observed in the numerical simulations is still governed by the local criterion despite its large radial extent.

Negative Rossby numbers, *i.e.* opposite sign of the zonal profile, have been calculated. The Rossby wave has the same characteristics than the ones obtained with positive Rossby numbers: s_c located close to a maximum of the zonal velocity, large radial extent, same speed over the whole shell and maximum of its amplitude in a negative peak of the zonal velocity.

The criterion (8) provides a theoretical critical Rossby number and the location of the barotropic instability for a given zonal velocity profile in the limit of negligible viscosity. According to the local criterion, the zonal velocity profile (1) imposed at the top of the model, and projected geostrophically in the equatorial plane, $U(s, \theta = \pi/2)$, becomes first unstable at the first (innermost) prograde jet (corresponding to a cylindrical radius $s = 0.25$) for a critical Rossby number of 0.0011 (denoted Ro_c^{loc} hereafter). The threshold of the first instability of the axisymmetric flow, denoted Ro_c^{nlin}, obtained with the numerical simulations are shown on figure 2. Despite the decrease of Ro_c^{nlin} with the Ekman number, Ro_c^{nlin} is still about 4 times larger than Ro_c^{loc} for $E = 10^{-6}$. Due to computational limit, it is not possible for us to carry out simulations at smaller E with a fully non-linear approach. In order to reach the asymptotic regime for the instability threshold we used a dedicated linear code described in B. The linear code calculates linear perturbation solutions to the momentum equation using the geostrophic profile U as the basic flow in the bulk of the fluid. The computational time is greatly reduced by the linear approach but is restricted to an analysis at the instability threshold. Note that we do not use the azimuthal symmetry as the choice of a given symmetry m_s may influence the position of the instability. The growing solutions obtained with the linear code displays very similar features (frequency, bidimensional structure, radial extent, location of the maximum amplitude in a retrograde jet) than the Rossby waves of the non-linear simulations. In figure 2 the threshold Ro_c^{lin} obtained with the linear approach is given together with the position of the unstable jet and the marginally stable mode m_c. The first unstable jet gets closer to the inner core as the Ekman number is decreased. Accordingly to the diminution of s_c, m_c becomes smaller. For the same Ekman number, the first unstable jet obtained with the linear code is closer to the axis than the one found with the fully non-linear code since the geostrophic zonal flow U is used in the linear approach, that is the inner jets have greater amplitude than in the non-linear approach. The discrepancy in the position and threshold of the instability between the local criterion and the numerical solutions disappears when very small viscosity is used ($E \leqslant 5 \times 10^{-7}$). From our linear computations we conclude that the theoretical criterion (8) is relevant to explain the onset of instability obtained numerically.

A.2 Model N

The instability takes the form of a $m = 2$ Rossby wave, which fills the entire gap. We calculate the frequency of the wave in the non-linear simulations to deduce s_c using the dispersion relation of the Rossby wave (6) and assuming

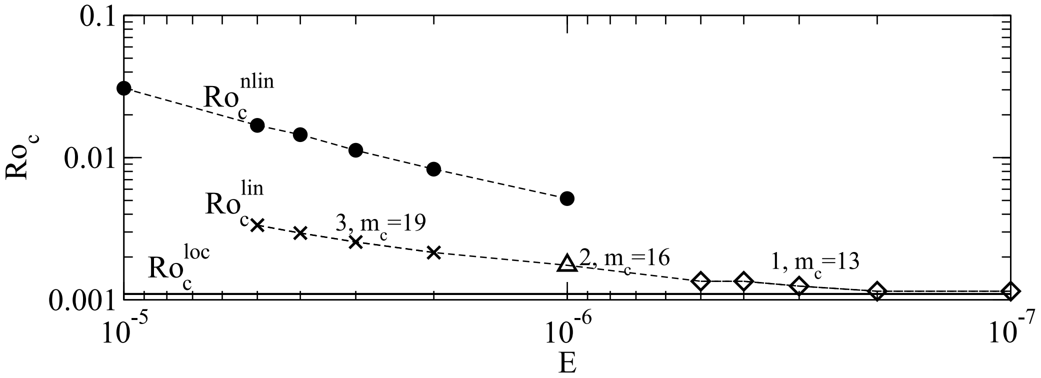

Figure 2: Critical Rossby number obtained from fully non-linear numerical simulations for the model J (Ro_c^{nlin}, circles) compared to the theoretical Rossby number obtained with the local instability criterion (8) using the geostrophic profile (1) $U(s, \theta = \pi/2)$ (Ro_c^{loc}, black line). The critical Rossby number obtained from the linear numerical calculation is also shown (Ro_c^{lin}, black symbols). The annotations close to the black symbols of Ro_c^{lin} stand for the number of the unstable prograde jet in the equatorial plane and the azimuthal wavenumber of the marginally stable mode: crosses: 3^{rd} jet unstable ($s_c = 0.5$) and $m_c = 19$; triangle: 2^{nd} jet unstable ($s_c = 0.38$) and $m_c = 16$; diamonds: 1^{st} jet unstable ($s_c = 0.25$) and $m_c = 13$.

that $k_s \approx m/s$. For $E = 10^{-5}$ and $E = 5 \times 10^{-6}$ we found $s_c = 0.53$, that is on the outward side of the positive peak of the zonal flow (located at $s = 0.36$) (see figure 5(b)). Using the local instability criterion with the geostrophic profile we obtain a critical Rossby number $Ro_c^{loc} = 0.026$ with the maximum of the gradient of vorticity $\partial_s \zeta$ located at $s = 0.308$. The numerics gives a larger critical radius compared to the theoretical prediction, likely a consequence of the viscous effects as reported for the model J . For $E = 10^{-5}$ ($E = 5 \times 10^{-6}$), the numerical critical Rossby number is $Ro_c^{nlin} = 0.0335$ ($Ro_c^{nlin} = 0.0325$ resp.). The critical Rossby numbers obtained with nonlinear code, Ro_c^{nlin}, are getting fairly close to the theoretical critical Rossby number Ro_c^{loc} when the Ekman number is decreased.

B Linear code used to compute the hydrodynamical instability threshold

In order to study the linear stability threshold at very low Ekman numbers, we designed a linear code derived from Gillet et al. (2011). This three-dimensional spherical code uses second order finite differences in radius and pseudo-spectral spherical harmonic expansion. The linear perturbation $\mathbf{u}$ of the imposed background flow $\mathbf{U}$ is time-stepped from a random initial field with the following equation :

$$\left(\frac{\partial}{\partial t} - \nabla^2\right)\mathbf{u} = -\left(\frac{2}{E}\mathbf{e_z} + \nabla \times \mathbf{U}\right) \times \mathbf{u} + \mathbf{U} \times \nabla \times \mathbf{u} - \nabla p, \qquad (21)$$

together with the continuity equation $\nabla \cdot \mathbf{u} = 0$, which allows us to eliminate the pressure term by using a poloidal-toroidal decomposition. The left hand side of equation 21 is treated with a semi-implicit Crank-Nicolson scheme, whereas the right hand side is treated as an explicit Adams-Bashforth term. Thanks to the cylindrical symmetry of the base flow $\mathbf{U}$, all azimuthal modes m of the perturbation $\mathbf{u}$ are independent, and we can compute them separately. The coupling with the background flow and the Coriolis force are handled in physical space, but a very fast implementation of the spherical harmonic transform (SHTns library) makes the code quite efficient.

In order to determine the stability threshold at $E = 10^{-7}$, we used 350 points in the radial direction, and spherical harmonics truncated at $l_{max} = 300$. We use no-slip boundary conditions.

References

Aubert, J., 2005. Steady zonal flows in spherical shell dynamos. J. Fluid Mech. 542, 53–67.

Aubert, J., Wicht, J., 2004. Axial vs. equatorial dipolar dynamo models with implications for planetary magnetic fields. Earth Planet. Sci. Lett. 221, 409–419.

Aurnou, J., Heimpel, M., Wicht, J., 2007. The effects of vigorous mixing in a convective model of zonal flow on the ice giants. Icarus 190, 110–126.

Avalos-Zuniga, R., Plunian, F., Radler, K.H., 2009. Rossby waves and α-effect. Geophys. Astrophys. Fluid Dyn. 103, 375–396.

Burton, M.E., Dougherty, M.K., Russell, C.T., 2009. Model of Saturn's internal planetary magnetic field based on Cassini observations. Plan. Space Sci. 57, 1706–1713.

Busse, F.H., 1975. A model of the geodynamo. Geophys. J. R. Astron. Soc. 42, 437–459.

Busse, F.H., 1976. A simple model of convection in the Jovian atmosphere. Icarus 29, 255–260.

Cho, J., Polvani, L.M., 1996. The morphogenesis of bands and zonal winds in the atmospheres on the giant outer planets. Science 273, 335–337.

Christensen, U.R., 2001. Zonal flow driven by deep convection in the major planets. Geophys. Res. Lett. 28.

Christensen, U.R., 2002. Zonal flow driven by strongly supercritical convection in rotating spherical shells. J. Fluid Mech. 470, 115–133.

Christensen, U.R., Aubert, J., 2006. Scaling properties of convection-driven dynamos in rotating spherical shells and application to planetary magnetic fields. Geophy. J. Int. 166, 97–114.

Christensen, U.R., Aubert, J., Cardin, P., Dormy, E., Gibbons, S., Glatzmaier, G.A., Grote, E., Honkura, Y., Jones, C., Kono, M., Matsushima, M., Sakuraba, A., Takahashi, F., Tilgner, A., Wicht, J., Zhang, K., 2001. A numerical dynamo benchmark. Phys. Earth Planet. Inter. 128, 25–34.

Christensen, U.R., Wicht, J., 2007. Numerical dynamo simulations, in: Schubert, G. (Ed.), Treatise on Geophysics. Elsevier, Amsterdam, pp. 245 – 282.

Connerney, J.E.P., Acuna, M.H., Ness, N.F., 1991. The magnetic field of Neptune. J. Geophys. Res. 96, 19023–+.

Dormy, E., 1997. Modélisation numérique de la dynamo terrestre. Ph.D. thesis. Institut de Physique du Globe de Paris.

Evonuk, M., Glatzmaier, G.A., 2004. 2D studies of various approximations used for modeling convection in giant planets. Geophys. Astrophys. Fluid Dyn. 98, 241–255.

Finlay, C.C., 2008. Waves in the presence of magnetic fields, rotation and convection, in: Cardin, P., Cugliandolo, L.F. (Eds.), Dynamos. Elsevier. volume 88 of *Les Houches Summer School Proceedings*, pp. 403 – 450.

Gillet, N., Schaeffer, N., Jault, D., 2011. Rationale and geophysical evidence for quasi-geostrophic rapid dynamics within the Earth's outer core. in press. Phys. Earth Planet. Inter. .

Glatzmaier, G.A., 2008. A note on constraints on deep-seated zonal winds inside Jupiter and Saturn. Icarus 196, 665–666.

Gómez-Pérez, N., Heimpel, M., 2007. Numerical models of zonal flow dynamos: an application to the ice giants. Geophys. Astrophys. Fluid Dyn. 101, 371–388.

Grote, E., Busse, F.H., 2001. Dynamics of convection and dynamos in rotating spherical fluid shells. Fluid Dyn. Res. 28, 349–368.

Gubbins, D., 2008. Implication of kinematic dynamo studies for the geodynamo. Geophys. J. Int. 173, 79–91.

Gubbins, D., Barber, C.N., Gibbons, S., Love, J.J., 2000. Kinematic dynamo action in a sphere. II. Symmetry selection. Proc. R. Soc. Lond. A 456, 1669–+.

Gubbins, D., Roberts, P.H., 1987. Geomagnetism. volume 2. Academic Press, London.

Guervilly, C., Cardin, P., 2010. Numerical simulations of dynamos generated in spherical Couette flows. Geophys. Astrophys. Fluid Dyn. 104, 221–248.

Guillot, T., 2005. The interiors of giant planets: models and outstanding questions. Annu. Rev. Earth Plan. Sci. 33, 493–530.

Guillot, T., Chabrier, G., Morel, P., Gautier, D., 1994. Nonadiabatic models of Jupiter and Saturn. Icarus 112, 354–367.

Guillot, T., Gautier, D., 2007. Giant planets, in: Schubert, G. (Ed.), Treatise on Geophysics. Elsevier, Amsterdam, pp. 439 – 464.

Guillot, T., Stevenson, D.J., Hubbard, W.B., Saumon, D., 2004. The interior of Jupiter, in: Bagenal, F., Dowling, T. E., & McKinnon, W. B. (Ed.), Jupiter. The Planet, Satellites and Magnetosphere, pp. 35–57.

Heimpel, M., Aurnou, J., Wicht, J., 2005. Simulation of equatorial and high-latitude jets on Jupiter in a deep convection model. Nature 438, 193–196.

Herbert, F., 2009. Aurora and magnetic field of Uranus. J. Geophys. Res. 114, A11206.

Holme, R., Bloxham, J., 1996. The magnetic fields of Uranus and Neptune: Methods and models. J. Geophys. Res. 101, 2177–2200.

Hubbard, W.B., Nellis, W.J., Mitchell, A.C., Holmes, N.C., McCandless, P.C., Limaye, S.S., 1991. Interior structure of Neptune - Comparison with Uranus. Science 253, 648–651.

Hubbard, W.B., Podolak, M., Stevenson, D.J., 1995. The interior of Neptune., in: D. P. Cruikshank, M. S. Matthews, & A. M. Schumann (Ed.), Neptune and Triton, pp. 109–138.

Ingersoll, A.P., Pollard, D., 1982. Motion in the interiors and atmospheres of Jupiter and Saturn - Scale analysis, anelastic equations, barotropic stability criterion. Icarus 52, 62–80.

Jones, C.A., Kuzanyan, K.M., 2009. Compressible convection in the deep atmospheres of giant planets. Icarus 204, 227 – 238.

Kaspi, Y., Flierl, G.R., Showman, A.P., 2009. The deep wind structure of the giant planets: Results from an anelastic general circulation model. Icarus 202, 525–542.

Kuo, H.L., 1949. Dynamic instability of two-dimensional nondivergent flow in a barotropic atmosphere. J. Atmos. Sci. 6, 105–122.

Liu, J., Goldreich, P.M., Stevenson, D.J., 2008. Constraints on deep-seated zonal winds inside Jupiter and Saturn. Icarus 196, 653–664.

Manneville, J., Olson, P., 1996. Banded convection in rotating fluid spheres and the circulation of the jovian atmosphere. Icarus 122, 242–250.

Moffatt, H.K., 1978. Magnetic field generation in electrically conducting fluids. University Press, Cambridge.

Nellis, W.J., Holmes, N.C., Mitchell, A.C., Hamilton, D.C., Nicol, M., 1997. Equation of state and electrical conductivity of "synthetic Uranus," a mixture of water, ammonia, and isopropanol, at shock pressure up to 200 GPa (2 Mbar). J. Chem. Phys. 107, 9096–9100.

Nellis, W.J., Weir, S.T., Mitchell, A.C., 1999. Minimum metallic conductivity of fluid hydrogen at 140 GPa (1.4 Mbar). Phys. Rev. B 59, 3434–3449.

Olson, P., Christensen, U., Glatzmaier, G.A., 1999. Numerical modeling of the geodynamo: Mechanisms of field generation and equilibration. J. Geophys. Res. 104, 10383–10404.

Pedlosky, J., 1979. Geophysical fluid dynamics. Springer-Verlag, New York.

Porco, C.C., West, R.A., McEwen, A., Del Genio, A.D., Ingersoll, A.P., Thomas, P., Squyres, S., Dones, L., Murray, C.D., Johnson, T.V., Burns, J.A., Brahic, A., Neukum, G., Veverka, J., Barbara, J.M., Denk, T., Evans, M., Ferrier, J.J., Geissler, P., Helfenstein, P., Roatsch, T., Throop, H., Tiscareno, M., Vasavada, A.R., 2003. Cassini imaging of Jupiter's atmosphere, satellites, and rings. Science 299, 1541–1547.

Redmer, R., Mattsson, T.R., Nettelmann, N., French, M., 2011. The phase diagram of water and the magnetic fields of Uranus and Neptune. Icarus 211, 798–803.

Reuter, K., Jenko, F., Tilgner, A., Forest, C.B., 2009. Wave-driven dynamo action in spherical magnetohydrodynamic systems. Phys. Rev. E 80, 056304–+.

Roberts, P., 2007. Theory of the geodynamo, in: Schubert, G. (Ed.), Treatise on Geophysics. Elsevier, Amsterdam, pp. 67 – 105.

Russell, C.T., Dougherty, M.K., 2010. Magnetic Fields of the Outer Planets. Space Sci. Rev. 152, 251–269.

Russell, C.T., Yu, Z.J., Khurana, K.K., Kivelson, M.G., 2001. Magnetic field changes in the inner magnetosphere of Jupiter. Adv. Space Res. 28, 897–902.

Sanchez-Lavega, A., Rojas, J.F., Sada, P.V., 2000. Saturn's zonal winds at cloud level. Icarus 147, 405–420.

Schaeffer, N., Cardin, P., 2005. Quasigeostrophic model of the instabilities of the Stewartson layer in flat and depth-varying containers. Phys. Fluids 17, 104111.

Schaeffer, N., Cardin, P., 2006. Quasi-geostrophic kinematic dynamos at low magnetic Prandtl number. Earth Planet. Sci. Lett. 245, 595–604.

Sromovsky, L.A., Fry, P.M., 2005. Dynamics of cloud features on Uranus. Icarus 179, 459–484.

Sromovsky, L.A., Fry, P.M., Dowling, T.E., Baines, K.H., Limaye, S.S., 2001. Coordinated 1996 HST and IRTF imaging of Neptune and Triton. III. Neptune's atmospheric circulation and cloud structure. Icarus 149, 459–488.

Stanley, S., Bloxham, J., 2006. Numerical dynamo models of Uranus' and Neptune's magnetic fields. Icarus 184, 556–572.

Stevenson, D.J., 1983. Planetary magnetic fields. Rep. Prog. Phys. 46, 555–557.

Stewartson, K., 1957. On almost rigid rotations. J. Fluid Mech. 3, 17–26.

Stewartson, K., 1966. On almost rigid rotations. part 2. J. Fluid Mech. 26, 131–144.

Tilgner, A., 2008. Dynamo Action with Wave Motion. Phys. Rev. Lett. 100, 128501–+.

Vasavada, A.R., Showman, A.P., 2005. Jovian atmospheric dynamics: an update after Galileo and Cassini. Rep. Prog. Phys. , 1935–1996.

Wicht, J., 2002. Inner-core conductivity in numerical dynamo simulations. Phys. Earth Planet. Inter. 132.

Wicht, J., Jones, C.A., Zhang, K., 2002. Instability of zonal flows in rotating spherical shells: an application to Jupiter. Icarus 155, 425–435.

Williams, G.P., 1978. Planetary circulations. I - Barotropic representation of Jovian and terrestrial turbulence. J. Atmos. Sci. 35, 1399–1426.

Williams, G.P., 2003. Jovian dynamics. Part III: multiple, migrating, and equatorial jets. J. Atmos. Sci. 60, 1270–1296.

Yano, J.I., Talagrand, O., Drossart, P., 2003. Outer planets: Origins of atmospheric zonal winds. Nature 421, 36.

Yu, Z.J., Leinweber, H.K., Russell, C.T., 2010. Galileo constraints on the secular variation of the Jovian magnetic field. J. Geophys. Res. 115, E03002.